Accurate stochastic simulation of non-elementary trimolecular reactions between closest particles

Taylor Kearney,[1, *] Ricardo Ruiz-Baier,[1, 2, 3, †] and Mark B. Flegg[1, ‡]

[1]*School of Mathematics, Monash University, 9 Rainforest walk, 3800 Clayton, Victoria, Australia.*
[2]*Universidad Adventista de Chile, Casilla 7-D Chillán, Chile.*
[3]*Institute for Computer Science and Mathematical Modeling,*
Sechenov First Moscow State Medical University, Moscow, Russia.
(Dated: August 8, 2025)

We study a system of diffusing point particles in which any triplet of particles reacts and is removed from the system when the relative proximity of the constituent particles satisfies a predefined condition. Proximity-based reaction conditions of this kind are commonly used in particle-based simulations of chemical kinetics to mimic bimolecular reactions, those involving just two reactants, and have been extensively studied. The rate at which particles react within the system is determined by the reaction condition and particulate diffusion. In the bimolecular case, analytic relations exist between the reaction rate and the distance at which particles react allowing modellers to tune the rate of the reaction within their simulations by simply altering the reaction condition. However, generalising proximity-based reaction conditions to trimolecular reactions, those involving three particles, is more complicated because it requires understanding the distribution of the closest diffusing particle to a point in the vicinity of a spatially dependent absorbing boundary condition. We find that in this case the evolution of the system is described by a nonlinear partial integro-differential equation with no known analytic solution, which makes it difficult to relate the reaction rate to the reaction condition. To resolve this, we use singular perturbation theory to obtain a leading-order solution and show how to derive an approximate expression for the reaction rate. We then use finite element methods to quantify the higher-order corrections to this solution and the reaction rate, which are difficult to obtain analytically. Leveraging the insights gathered from this analysis, we demonstrate how to correct for the errors that arise from adopting the approximate expression for the reaction rate, enabling for the construction of more accurate particle-based simulations than previously possible.

I. INTRODUCTION

Transport-dependent phenomena are ubiquitous in many chemical systems, particularly in intracellular environments. The most fundamental example of molecular transport is the thermally driven random motion that results in a net movement from regions of high concentration to those with lower concentrations, known as diffusion [1]. Due to its fundamental nature, diffusion is both ubiquitous and essential in biology [2]. It plays a central role in the operation of microorganisms [3] and is vital in numerous cellular processes, including metabolism [4, 5] and signalling [6–8]. More broadly, diffusion facilitates the mixing of reactants on small spatial scales, promoting the molecular collisions necessary for biochemical reactions to occur [9, 10]. If reactant diffusion is sufficiently slow, it largely determines the reaction rate, leading to a *diffusion-limited* reaction. This has driven significant interest in diffusion-limited reactions and their kinetics have been extensively studied at various levels of fidelity.

Many models consider the kinetics of diffusion-limited reactions to be deterministic, assuming that the reactants can be well approximated using continuous concentrations. These deterministic models use either ordinary differential equations (ODEs) to investigate only the temporal evolution of reactant concentrations [11, 12], or employ partial differential equations (PDEs), known as reaction-diffusion equations, to explicitly incorporate reactant diffusion [13, 14]. Although such models have been widely studied, they provide an inadequate description of many biological systems

---

whose kinetics are inherently stochastic [15–18] due to their molecular origins. Moreover, molecular populations are often so low or so spatially localised that meaningful concentrations cannot be defined [19, 20].

These shortcomings have motivated the development of a range of models, summarised in Figure I.1 and reviewed in [21], that incorporate stochastic effects as a core component. The Chemical Master Equation (CME) [22, 23] is one of the earliest and most influential models in this class. It is a system of coupled ordinary differential equations that describes the time evolution of the probability mass function for the system to contain a specific number of molecules of each species at time t. In general, the CME very difficult to solve analytically [24] and so the stochastic time evolution of molecular populations is typically simulated using Gillespie's stochastic simulation algorithm (SSA) [25, 26]. The CME, and hence the SSA, only applies to spatially homogeneous, or well-mixed chemical systems, but it can be extended to spatially heterogeneous systems by dividing the domain into spatially homogeneous voxels or compartments that are coupled through diffusive transfers [27, 28].

This approach leads to a model commonly referred to as the reaction-diffusion master equation (RDME) [29], which discretises space in the same manner, but does not necessarily rely on the SSA to evolve voxel populations [30–34]. The RDME provides a computationally efficient way to incorporate spatial dependence in stochastic models. However, the size of the voxels is inherently limited by the assumption that they are well mixed. In many cases, finer spatial resolution is required to accurately capture the behaviour of the system, leading to more computationally intensive RDME approaches [35].

Perhaps the most natural choice for models of reaction-diffusion systems are those that aim to faithfully replicate the actual dynamics of the system by explicitly treating molecules as individuals undergoing a reaction-diffusion process. Molecular dynamics simulations [36] take this notion to the extreme, attempting to accurately reproduce the physical system with atomic detail. Although they are highly accurate, these simulations can be prohibitively expensive due to the sheer number of degrees of freedom that must be modelled; many of which arise from the need to explicitly track solvent molecules, account for numerous possible interactions, and capture intramolecular timescales [37].

To partially mitigate these computational challenges, particle-based models leverage simplifying assumptions to improve efficiency [21, 38] and are widely used in the literature [39]. These models avoid the explicit treatment of solvent molecules and describe the relevant reactants as points undergoing isotropic diffusion on a continuous domain. In the absence of spatial morphology for individual molecules, these approaches typically favour idealised proximity-based (and sometimes energy-potential-based) reaction conditions that are simple to implement, making such simulations feasible to run on personal computing hardware.

This approach was largely inspired by Smoluchowski [40], who postulated that bimolecular reactions could be modelled by assuming that two molecules undergo a reaction if they come within a predefined distance σ, called the *reaction radius*. Although simple, Smoluchowski's reaction condition has proven remarkably robust and forms the basis of many prominent software packages for particle-based simulation of reaction-diffusion systems, including Green's function reaction dynamics (GFRD) [41, 42], enhanced Green's function reaction dynamics (eGFRD) [43, 44], Smoldyn [45], and ReaDDy [46].

For a bimolecular reaction between two chemical species A and B, Smoluchowski's model imposes that the rate of reaction is simply the number of successful 'collisions' between molecules of A and B at a distance σ per unit time. This reaction rate is inherently stochastic because it depends on the motion of individual diffusing molecules. However, if we were to average the reaction rates obtained from a large ensemble of independent molecules of A surrounded by molecules of B, then the expected reaction rate should converge to the corresponding macroscopic rate. This provides a matching condition that can be used to determine the currently unknown reaction radius σ.

To derive this condition, we consider a system of extremely large (relative to molecular sizes) volume V that contains a single isolated molecule of A surrounded by molecules of B. For this system, the joint probability density $P_S(r_1, t)$ for finding a molecule of B, that has never collided with A, at a given position at time t only depends on the radial distance r_1 between this molecule and A and evolves according to the diffusion equation,

$$\frac{dP_S(r_1, t)}{dt} = \frac{\hat{D}_1}{r_1^2} \frac{\partial}{\partial r_1} \left(r_1^2 \frac{\partial P_S(r_1, t)}{\partial r_1} \right), \tag{I.1}$$

where $\hat{D}_1 = D_0 + D_1$ is the relative diffusion coefficient between molecules A and B (the sum of their diffusion coefficients). Smoluchowski's reaction condition specifies that molecules of B must be removed from the system at a distance $r_1 = \sigma$ from A which manifests as an absorbing boundary condition

$$P_S(r_1, t) = 0 \text{ on } r_1 = \sigma. \tag{I.2}$$

The expected reaction rate is given by the diffusive flux over this boundary which rapidly approaches the pseudo-equilibrium value [40, 47]

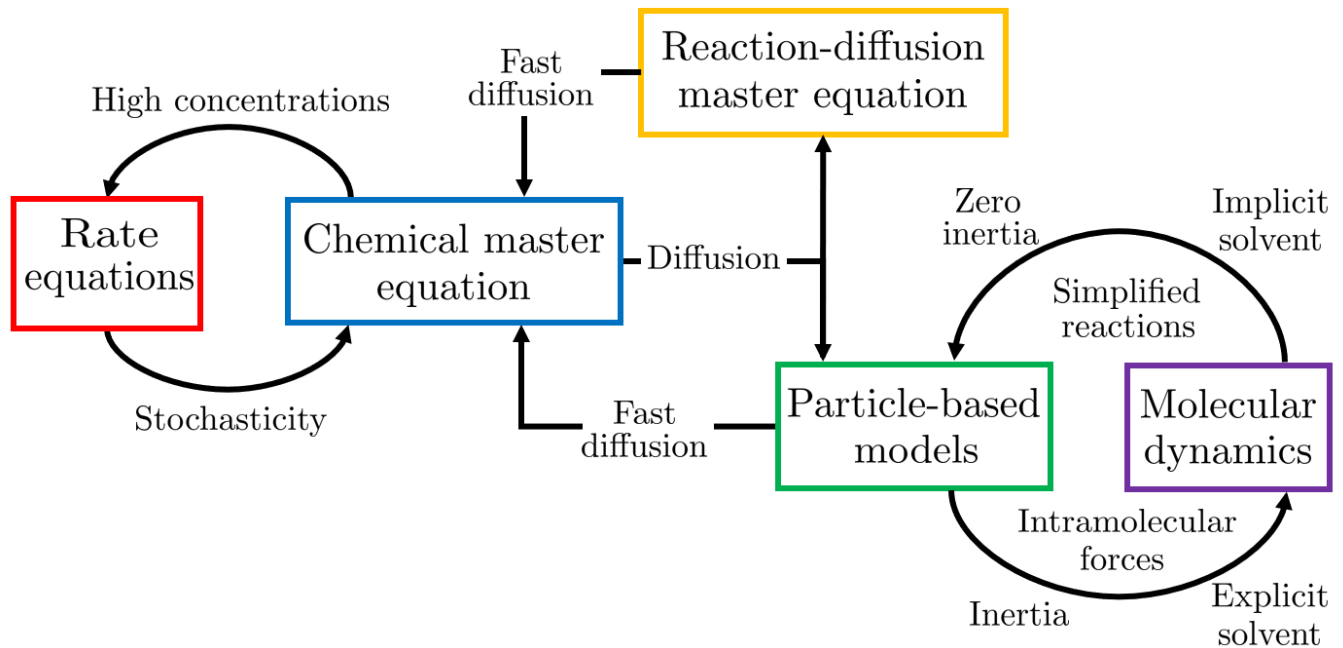$$K_S(\sigma) = \frac{k_2}{V} = \frac{4\pi\sigma\hat{D}_1}{V}, \tag{I.3}$$

FIG. I.1: A summary of the relationships between models of biochemical reactions. The models increase in complexity and physical realism from left to right. The rightward arrows indicate the additional physical mechanisms required to progress to a more detailed model. Conversely, the leftward arrows represent the limit in which a more complicated model reduces to a simpler one. Particle-based models are obtained from molecular dynamics models by assuming reactants undergo diffusive motion as a result of their collisions with implicit solvent molecules and replacing complicated intramolecular interactions with simplified reaction conditions. Particle-based models are an alternative to the reaction-diffusion master equation (RDME) in that they account for reactant diffusion neglected by the Chemical Master Equation (CME). This figure was adapted from [21] which provides a detailed review of the relationships summarised here.

where k_2 is the bimolecular rate of reaction (first passage rate for a collision). Notice that Equation (I.3) assumes that

$$\lim_{r_1 \to \infty} P_S(r_1, t) = \frac{1}{V}. \tag{I.4}$$

This requires that the molecules of B are initially well mixed (distributed uniformly at random), and that the absorption of molecules on $r_1 = \sigma$ does not perturb the probability density far from this boundary.

Equation (I.3) gives the reaction rate for a single molecule of A per molecule of B and is used to determine σ based on a known second-order rate constant k_2. To recover the macroscopic reaction rate we assume that molecules of A can be considered independently, so that the expected reaction rate for a system containing multiple molecules is given by Equation (I.3) multiplied the number of molecules of A and the number of molecules of B. Note that often Equation (I.3) is instead multiplied by the concentration of A (rather than the number of A molecules), since for an elementary bimolecular reaction the resulting rate of change for the concentration can be directly compared to the macroscopic rate given by the law of mass action, which states the rate is given by the product of the reactant concentrations multiplied by the second-order rate constant k_2 associated with the reaction.

The validity of Smoluchowski's reaction condition, and the many derivatives it has inspired [20, 48, 49], is contingent upon the distance at which molecules interact being sufficiently small. Specifically, for Smoluchowski's model, the reaction radius σ must be sufficiently small when compared to the expected separation between the molecules [50]. In other words, we require the system to be sufficiently sparse or the affinity of A for B to be sufficiently low so that the associated reaction radius is small. Collins and Kimball [48] alleviate this requirement by supposing that not every collision results in a reaction which amounts to replacing Smoluchowski's absorbing boundary in Equation (I.2) with a partially reflective condition. Similarly, Doi [49] allows reactants to approach arbitrarily close to each other and only requires that reactions occur at a fixed rate per unit time once reactants are separated by a distance less than the analogous reaction radius parameter. These alternative reaction conditions enable the distance at which molecules react to be increased for a fixed reaction rate when compared to Smoluchowski's reaction condition, but in

each case the reaction condition is still fundamentally a proximity-dependent interaction between molecules that can be summarised by a single parameter, analogous to σ, which determines the spatial scale at which interactions occur [51]. Moreover, for our assumptions regarding the independence of reactants of the same species to be accurate, the interaction distance must still be small regardless of the reaction condition adopted.

Flegg [51] demonstrated that proximity-based reaction conditions equivalent to Smoluchowski's can also be applied to higher-order reactions (those involving more than two reactants), while Kearney and Flegg [50] demonstrated proximity-based trimolecular reaction conditions can produce *non-elementary* kinetics that cannot be described by the law of mass action. In this article, we consider a trimolecular reaction of the general form

$$A + B + C \longrightarrow C, \tag{I.5}$$

which we suppose is mediated by a proximity-based reaction condition akin to those developed by Kearney and Flegg in [50].

To describe the reaction condition, we follow Flegg [51] and generalise the notion of reactant proximity to trimolecular reactions by introducing two new coordinates, $\boldsymbol{\eta}_1$ and $\boldsymbol{\eta}_2$. We will discuss this coordinate system in greater detail in Section II, so for now it is sufficient to note that $\boldsymbol{\eta}_1$ describes the separation between a particular pair of A and B molecules. While $\boldsymbol{\eta}_2$ captures the relative proximity of a third molecule C to this pair. Due to the radial symmetry of the system, proximity-based reaction conditions for the reaction in Equation (I.5) can be expressed naturally as functions of the radial coordinates $r_i \equiv ||\boldsymbol{\eta}_i||$. Smoluchowski's original bimolecular condition can be extended in a straightforward manner to our trimolecular reaction by considering a reaction boundary that extends only a small distance in both r_1 and r_2. In this case, the system will reach a pseudo-equilibrium that returns trimolecular mass-action kinetics. However, a trimolecular system contains an additional spatial degree of freedom, namely r_2, when compared to a bimolecular system, which offers an opportunity to consider more elaborate reaction conditions. Specifically, we can consider reaction conditions where the separation, r_1, at which the pair of A and B molecules reacts is mediated by the distance, r_2, to the molecule of C that is closest to this pair. In this case, the reaction condition still manifests as an absorbing boundary $\partial\Omega_R$ that is always small in the $\boldsymbol{\eta}_1$ direction, meaning molecules of A and B must be close if they are to react, but now can be comparatively long in the $\boldsymbol{\eta}_2$ direction so the molecule of C involved in the reaction is not necessarily close to A and B.

The expected reaction rate for the trimolecular system is calculated in the same way as it is for a bimolecular system and is determined by the total flux of the probability density across $\partial\Omega_R$. However, now we are concerned with the probability density for finding the state, where each state consists of the pair of A and B molecules and a particular molecule of C, associated with the C molecule with the minimum r_2 value. That is, we must restrict our attention to the state that contains the molecule of C that is closest to A and B, since this state will be the first to satisfy the reaction condition. For all but the simplest choices of $\partial\Omega_R$, determining this probability density analytically is very difficult, and thus it is not possible to derive an analytic expression for the reaction rate in general. To avoid this issue, Kearney and Flegg [50] (implicitly) utilised singular perturbation theory to derive a leading-order solution for the steady-state probability density near $\partial\Omega_R$. They then demonstrated, via a particle-based simulation, that the total flux across this boundary can be approximated by just the diffusive flux of this leading-order solution in the $\boldsymbol{\eta}_1$ direction. This approximation yields an analytic expression, analogous to Smoluchowski's in Equation (I.3), which relates the reaction rate to the reaction boundary and thus allows us to match $\partial\Omega_R$ to any given reaction rate.

Unfortunately, this approximation will yield a reaction boundary that does not exactly reproduce the desired reaction rate when incorporated into a simulation, and instead small errors are observed between the simulated and desired rates. These errors are the result of neglecting second-order contributions to the diffusive flux in the $\boldsymbol{\eta}_1$ direction across $\partial\Omega_R$ and entirely neglecting the flux across this boundary in the $\boldsymbol{\eta}_2$ direction that arises from the relative motion of C molecules. That is, the simulated rate reflects the exact flux across $\partial\Omega_R$ which in general differs from what we are led to expect when adopting the approximate reaction rate. In this article, we seek to address these shortcomings by examining the accuracy of this approximation for the functional form of $\partial\Omega_R$ considered by Kearney and Flegg [50].

We begin in Section II by deriving a nonlinear partial integro-differential equation that governs the evolution of the probability density to find the state associated with the closest molecule of C and whose analytic solution is unknown for arbitrary $\partial\Omega_R$. Although we consider its direct application to the optimisation of particle-based simulations, this equation has broader interest in applied mathematics. This work is, in part, a continuation of Redner and Ben-Avraham's [52] in which they examined the distance of the closest molecule to a static trap. Redner and Ben-Avraham generalised the three-dimensional Hertz distribution [53], which assumes that both the trap and surrounding molecules are static, but only considered a constant reaction radius. In contrast, we consider the case where this radius varies with r_2. Moreover, since all reactants undergo diffusion it is tempting to compare our results to the case where the trap is also mobile, which has been studied in lower dimensional systems [54, 55]; however, such studies are typically concerned with the correlations that arise between reactants [56–58], whereas we restrict our attention to the mean-field behaviour of the system.

We use singular perturbation theory [59, 60] to derive a leading-order solution for the probability density to find the closest molecule, and demonstrate how to use this solution to construct the aforementioned approximation to the steady-state reaction rate. Ideally, we would continue with this analysis to derive the higher-order corrections to the solution, and hence to the reaction rate, but the particular form of the problem makes this challenging. Thus, to quantify these corrections we turn to numerical methods, which are the other 'principal approach for solving singular perturbation problems' [59] and are commonly used to investigate singularly perturbed reaction-diffusion systems [61–63]. Since both the probability density and the flux of this quantity are of interest, in Section III we adopt a mixed-primal variational formulation of the problem and present the corresponding finite element discretisation, which uses a continuous interior penalty scheme for the primal equation. The associated finite element solutions are then used to probe the higher-order corrections to the probability density and the reaction rate in Subsection IV A. Finally, in Subsection IV B we demonstrate how to alter the reaction boundary so that it more accurately reproduces the desired reaction rate, enabling the development of more accurate particle-based simulations without sacrificing the convenience afforded by an analytic expression.

II. THE EVOLUTION OF THE CLOSEST MOLECULE

To model the trimolecular reaction in Equation (I.5) we consider a domain Ω of volume V, where V is finite but very large, that contains the three distinct chemical species, A, B and C, whose molecules are all initially well mixed (distributed uniformly at random) within Ω. It is convenient to assume that the system contains a single molecule of A and B, and $N_C = cV$ molecules of C where c is a well-mixed concentration of C molecules. In essence, we are assuming that distinct pairs of A and B molecules can be treated independently, which, just as in the bimolecular case, is a good approximation so long as molecules only interact on small spatial scales. Furthermore, we assume that the molecules diffuse independently within the volume. Under these assumptions, the system contains N_C distinct states, where each state contains the single molecule of A, the single molecule of B and a particular C molecule.

To understand the dynamics of this system, it is instructive to initially restrict our attention to a single of the N_C distinct states. We will use D_i and $\mathbf{x}_i$, where $i = 0, 1, 2$, to denote the diffusion constant and the 3-dimensional position of the molecules of A, B and C respectively. Since we are primarily concerned with the molecules' relative proximity it is convenient to transform the coordinate system into diffusive Jacobi coordinates or separation coordinates,

$$\boldsymbol{\eta}_0 = \bar{\boldsymbol{x}}_2 \quad \text{and} \tag{II.1a}$$

$$\boldsymbol{\eta}_i = \boldsymbol{x}_i - \bar{\boldsymbol{x}}_{i-1}, \quad i = 1, 2, \quad \text{where}, \tag{II.1b}$$

$$\bar{\boldsymbol{x}}_i = \frac{\sum_{j=0}^{i} \boldsymbol{x}_j D_j^{-1}}{\sum_{k=0}^{i} D_k^{-1}}, \tag{II.1c}$$

is the *centre of diffusion* of the first $i + 1$ molecules and is analogous to the centre of mass except that the positions are weighted by their inverse diffusion coefficients rather than their masses. These weights are chosen so that, under the coordinate transformation from $\boldsymbol{x}_i$ to $\boldsymbol{\eta}_i$, the Laplacian term in the diffusion equation remains diagonal, with no mixed derivative terms. That is, each vector $\boldsymbol{\eta}_i$ diffuses independently. This property is explored in greater detail by Flegg [51].

Since $\boldsymbol{\eta}_0$ is the centre of diffusion of the three molecules, changes in it correspond to translations of the state within the domain. That is, varying $\boldsymbol{\eta}_0$ does not change the relative proximity of the molecules in the current state, so we will only consider initial and boundary conditions that are independent of $\boldsymbol{\eta}_0$. As a result, the joint probability density to find the unreacted state is also independent of $\boldsymbol{\eta}_0$ and we will be concerned exclusively with $\boldsymbol{\eta}_1$ and $\boldsymbol{\eta}_2$. As shown in Figure II.1, $\boldsymbol{\eta}_1$ describes the separation between A and B as by definition $\bar{\boldsymbol{x}}_0 = \boldsymbol{x}_0$, and $\boldsymbol{\eta}_2$ describes the separation between C and the centre of diffusion, $\bar{\boldsymbol{x}}_1$, of A and B. In addition, $\boldsymbol{\eta}_1$ and $\boldsymbol{\eta}_2$ undergo independent linear diffusion with diffusion constants

$$\hat{D}_1 = D_1 + \bar{D}_0 \quad \text{and} \quad \hat{D}_2 = D_2 + \bar{D}_1, \tag{II.2}$$

respectively, where $\bar{D}_j$ is the diffusion constant associated with $\bar{\boldsymbol{x}}_j$

$$\bar{D}_j = \frac{1}{\sum_{i=0}^{j} D_i^{-1}}. \tag{II.3}$$

The joint probability density, $P(\boldsymbol{\eta}, t)$, to find the molecules in an unreacted state at time t is given by the diffusion equation

$$\frac{\partial P(\boldsymbol{\eta}, t)}{\partial t} = \left[\sum_{i=1}^{2} \hat{D}_i \hat{\nabla}_i^2 \right] P(\boldsymbol{\eta}, t), \tag{II.4}$$
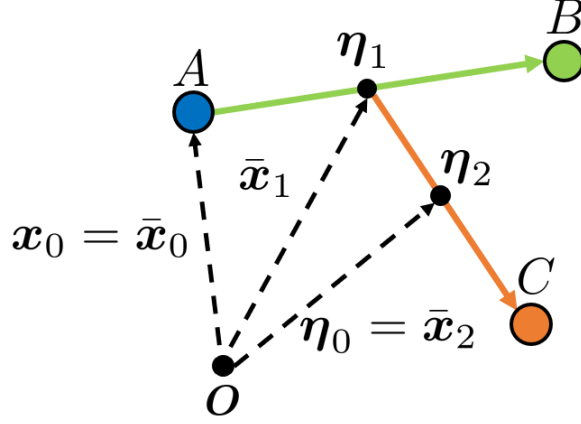
FIG. II.1: The diffusive Jacobi coordinates for a system containing three molecules. The coordinate $\boldsymbol{\eta}_1$ describes the separation between the first two molecules, labelled A and B, while $\boldsymbol{\eta}_2$ describes the separation of the third molecule C from the centre of diffusion of A and B which we denote $\bar{\boldsymbol{x}}_1$ and is defined in Equation (II.1c). Finally, $\boldsymbol{\eta}_0$ is the centre of diffusion of the three molecules ($\bar{\boldsymbol{x}}_2$) and changes in this coordinate correspond to translations of the state.

where $\boldsymbol{\eta} = \{\boldsymbol{\eta}_1, \boldsymbol{\eta}_2\}$ is the state vector for the system and $\hat{\nabla}_i^2$ denotes the Laplacian with respect to the coordinates of $\boldsymbol{\eta}_i$. Since the system contains only a single molecule of A and B, the entire system is absorbed when a reaction occurs. For the trimolecular reaction in Equation (I.5) a general proximity-based reaction condition can be defined as the absorbing boundary

$$\partial\Omega_R = \{(\boldsymbol{\eta}_1, \boldsymbol{\eta}_2) : r_1 = f(r_2)\}, \tag{II.5}$$

where $0 \leq f(r_2) \leq \sigma_{\max}$ is a monotonically decreasing function of r_2 (recall that $r_i = ||\boldsymbol{\eta}_i||$) and $\sigma_{\max}$ is a small positive constant relative to the support of f. Furthermore, we assume that $\sigma_{\max}$ is small enough that:

1. The reaction is diffusion-limited, which requires the timescale for molecules of A and B to come into contact, characterised by $V/(\hat{D}_1\sigma_{\max})$, to be much longer than the timescale on which they react once in contact.

2. Pairs of A and B molecules can be considered independently, which requires that $\sigma_{\max}^3 a \ll 1$ and $\sigma_{\max}^3 b \ll 1$, where a and b denote the respective reactant concentrations.

3. For r_2 of $O(1)$ or greater, we have $\hat{D}_2\sigma_{\max}^2/(\hat{D}_1 r_2^2) \ll 1$, which we require for the forthcoming singular perturbation analysis to be valid.

According to this reaction boundary, the distance at which the molecules of A and B react is mediated by their relative proximity to the molecule of C rather than being fixed as it is in the bimolecular case. Moreover, the monotonic decay of the reaction boundary reflects the physical notion that reactions become more likely as the relative proximity between the three molecules reduces. In the case where the system contains a single molecule of C its evolution is governed by Equation (II.4) subject to the inner boundary condition

$$P(\boldsymbol{\eta} \in \partial\Omega_R, t) = 0. \tag{II.6}$$

However, in general this particular state will not be the first to cross $\partial\Omega_R$ and so to model the full system, we must consider N_C distinct states; one for each combination of A, B and a particular C molecule as shown in Figure II.2.

For any single particular state, $\boldsymbol{\eta}_1$ and $\boldsymbol{\eta}_2$ diffuse independently, so that the joint probability density can be written as, $P(\boldsymbol{\eta}, t) = P_1(\boldsymbol{\eta}_1, t) P_2(\boldsymbol{\eta}_2, t)$, where the probability densities P_1 and P_2 evolve according to

$$\left[\frac{\partial}{\partial t} - \hat{D}_1\hat{\nabla}_1^2\right] P_1(\boldsymbol{\eta}_1, t) \equiv \mathcal{L}_1 P_1(\boldsymbol{\eta}_1, t) = 0 \quad \text{and} \tag{II.7a}$$

$$\left[\frac{\partial}{\partial t} - \hat{D}_2\hat{\nabla}_2^2\right] P_2(\boldsymbol{\eta}_2, t) \equiv \mathcal{L}_2 P_2(\boldsymbol{\eta}_2, t) = 0. \tag{II.7b}$$

Here $\mathcal{L}_1$ and $\mathcal{L}_2$ are diffusion operators on the 3-dimensional spaces defined by $\boldsymbol{\eta}_1$ and $\boldsymbol{\eta}_2$, respectively. Since every state shares the same molecule of B, all states lie on manifolds of constant $\boldsymbol{\eta}_1$ and the specific instance of $\boldsymbol{\eta}_1$ diffuses
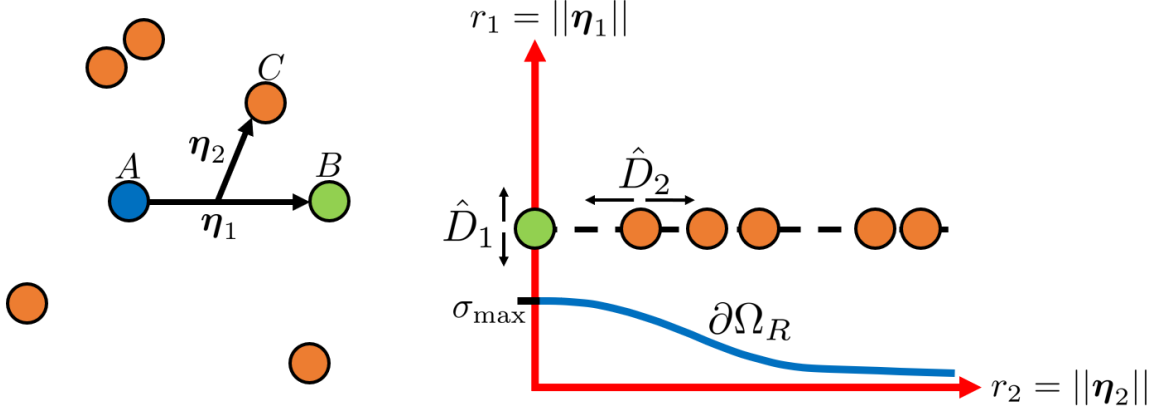
FIG. II.2: The state space for a system that contains a single molecule of A (the blue point), a single molecule of B (the green point) and five molecules of C (the orange points). Each combination of A and B with a particular molecule of C gives a point within the state space on the right, shown by the orange points. The position of the B molecule relative to the A molecule defines a manifold of constant $\boldsymbol{\eta}_1$ that all states lie on. This manifold diffuses in $\boldsymbol{\eta}_1$ in accordance with Equation (II.7a) and the states on the manifold diffuse independently in $\boldsymbol{\eta}_2$ according to Equation (II.7b). The reaction boundary $\partial\Omega_R$, defined in Equation (II.5), is shown as the blue curve and attains a maximum value of $\sigma_{\max}$ at $r_2 = 0$. The first state to cross $\partial\Omega_R$ will be absorbed.

according to Equation (II.7a). On this manifold, states diffuse independently in the 3-dimensional space defined by $\boldsymbol{\eta}_2$ in accordance with Equation (II.7b). The first state incident on the inner boundary $\partial\Omega_R$ will cause the entire system to be absorbed, and since f is monotonic, this state will be the one with the minimum r_2. That is, we wish to know the dynamics of the state that contains the molecule of C that is closest to the centre of diffusion of A and B.

If the system is well mixed, we can assume that the $\boldsymbol{\eta}_2$ coordinates of the N_C states are uniformly and independently distributed throughout Ω. Now consider a particular molecule of C and let $\boldsymbol{Z}_2$ denote the event that this particular molecule is associated with the minimum r_2 when compared with any other C molecule in the system. Since the molecules are well mixed, the probability that an arbitrary C molecule has the minimum r_2 at time t is

$$\Pr(\boldsymbol{Z}_2, t) = \frac{1}{N_C}. \tag{II.8}$$

The probability that a particular molecule of C has the minimum r_2 at time t given it has a known $\boldsymbol{\eta}_2$, is equal to the probability that all the other $N_C - 1$ molecules of C lie outside a spherical region V_2, of radius r_2 that is centred on the origin. That is,

$$\Pr(\boldsymbol{Z}_2, t | \boldsymbol{\eta}_2) = \left[1 - \int_{V_2} P_2(\boldsymbol{\eta}_2', t)\, dV_2'\right]^{N_C - 1}, \tag{II.9}$$

where dV_2' is an elemental volume for the coordinates of $\boldsymbol{\eta}_2'$. The probability density, $P(\boldsymbol{\eta}_2, t | \boldsymbol{Z}_2)$, for finding a particular molecule of C at $\boldsymbol{\eta}_2$ at time t, given that it has the smallest r_2 of any molecule of C in the system, can be found by using Bayes' theorem in combination with Equations (II.8) and (II.9),

$$P(\boldsymbol{\eta}_2, t | \boldsymbol{Z}_2) = N_C P_2(\boldsymbol{\eta}_2, t) \left[1 - \int_{V_2} P_2(\boldsymbol{\eta}_2', t)\, dV_2'\right]^{N_C - 1}. \tag{II.10}$$

The system is very large and, in the limit that V—and hence N_C—tends to infinity, $P(\boldsymbol{Z}_2, t)$ goes to zero in accordance with Equation (II.8). To ensure we take the appropriate limit in Equation (II.10) we define the scaled probability densities

$$\Phi(\boldsymbol{\eta}_2, t) = \frac{P(\boldsymbol{\eta}_2, t | \boldsymbol{Z}_2)}{c} \quad \text{and} \tag{II.11a}$$

$$\varphi(\boldsymbol{\eta}_2, t) = \frac{N_C P_2(\boldsymbol{\eta}_2, t)}{c}, \tag{II.11b}$$

which when substituted into Equation (II.10) give,

$$\Phi\left(\boldsymbol{\eta}_2, t\right) = \varphi\left(\boldsymbol{\eta}_2, t\right) \left[1 - \frac{c}{N_C} \int_{V_2} \varphi\left(\boldsymbol{\eta}_2', t\right) dV_2'\right]^{N_C - 1}. \tag{II.12}$$

Taking the limit $N_C \to \infty$ in Equation (II.12) gives

$$\Phi\left(\boldsymbol{\eta}_2, t\right) = \varphi\left(\boldsymbol{\eta}_2, t\right) \exp\left(-c \int_{V_2} \varphi\left(\boldsymbol{\eta}_2', t\right) dV_2'\right), \tag{II.13}$$

and then using Equation (II.7b), we find that $\Phi\left(\boldsymbol{\eta}_2, t\right)$ evolves according the advection-diffusion equation

$$\frac{\partial \Phi\left(\boldsymbol{\eta}_2, t\right)}{\partial t} = \hat{D}_2 \hat{\nabla}_2^2 \Phi\left(\boldsymbol{\eta}_2, t\right) + \hat{D}_2 \hat{\nabla}_2 \cdot \left(4\pi r_2^2 c\phi\left(\boldsymbol{\eta}_2, t\right) \Phi\left(\boldsymbol{\eta}_2, t\right) \hat{\boldsymbol{r}}_2\right), \tag{II.14}$$

where $\hat{\boldsymbol{r}}_2$ is the unit outward facing normal vector of a sphere of radius r_2 centred on the origin. A derivation of this result can be found in Appendix A.

Equation (II.14) can be written entirely in terms of $\Phi\left(\boldsymbol{\eta}_2, t\right)$ by noting that $P\left(\boldsymbol{Z}_2, t|\boldsymbol{\eta}_2\right)$ is also equal to the probability that the closest molecule is not inside the spherical region V_2. That is, in addition to Equation (II.9) we must also have

$$\mathrm{Pr}\left(\boldsymbol{Z}_2, t|\boldsymbol{\eta}_2\right) = 1 - \int_{V_2} P\left(\boldsymbol{\eta}_2', t|\boldsymbol{Z}_2\right) dV_2' = \int_{r_2}^{\infty} P\left(\boldsymbol{\eta}_2', t|\boldsymbol{Z}_2\right) 4\pi r_2'^2 \, \mathrm{d}r_2', \tag{II.15}$$

Bayes Theorem then gives

$$P_2\left(\boldsymbol{\eta}_2, t\right) = \frac{P\left(\boldsymbol{\eta}_2, t|\boldsymbol{Z}_2\right) \mathrm{Pr}\left(\boldsymbol{Z}_2, t\right)}{\mathrm{Pr}\left(\boldsymbol{Z}_2, t|\boldsymbol{\eta}_2\right)}, \tag{II.16}$$

from which we conclude

$$c\varphi\left(\boldsymbol{\eta}_2, t\right) = \frac{\Phi\left(\boldsymbol{\eta}_2, t\right)}{\int_{r_2}^{\infty} \Phi\left(\boldsymbol{\eta}_1', t\right) 4\pi r_2'^2 \, \mathrm{d}r_2'}. \tag{II.17}$$

Substituting Equation (II.17) into Equation (II.14), and then using Equation (II.11a), we arrive at the governing equation for $P\left(\boldsymbol{\eta}_2, t|\boldsymbol{Z}_2\right)$

$$\frac{\partial P\left(\boldsymbol{\eta}_2, t|\boldsymbol{Z}_2\right)}{\partial t} = \hat{D}_2 \hat{\nabla}_2^2 P\left(\boldsymbol{\eta}_2, t|\boldsymbol{Z}_2\right) + \hat{D}_2 \hat{\nabla}_2 \cdot \left(\frac{r_2^2 \left(P\left(\boldsymbol{\eta}_2, t|\boldsymbol{Z}_2\right)\right)^2 \hat{\boldsymbol{r}}_2}{\int_{r_2}^{\infty} P\left(\boldsymbol{\eta}_2', t|\boldsymbol{Z}_2\right) r_2'^2 \, \mathrm{d}r_2'}\right). \tag{II.18}$$

Finally, we note that since $\boldsymbol{\eta}_1$ diffuses independently of $\boldsymbol{\eta}_2$, the evolution of the joint probability density $P\left(\boldsymbol{\eta}, t|\boldsymbol{Z}_2\right)$ for finding the separation of the state with the minimum value of r_2 is governed by,

$$\frac{\partial P\left(\boldsymbol{\eta}, t|\boldsymbol{Z}_2\right)}{\partial t} = \left[\sum_{i=1}^{2} \hat{D}_i \hat{\nabla}_i^2\right] P\left(\boldsymbol{\eta}, t|\boldsymbol{Z}_2\right) + \hat{D}_2 \hat{\nabla}_2 \cdot \left(\frac{r_2^2 \left(P\left(\boldsymbol{\eta}, t|\boldsymbol{Z}_2\right)\right)^2 \hat{\boldsymbol{r}}_2}{\int_{r_2}^{\infty} P\left(\boldsymbol{\eta}_1, \boldsymbol{\eta}_2', t|\boldsymbol{Z}_2\right) r_2'^2 \, \mathrm{d}r_2'}\right). \tag{II.19}$$

The linear diffusion terms in Equation (II.19) describe the independent Brownian motion of $\boldsymbol{\eta}_1$ and $\boldsymbol{\eta}_2$, while the advection towards $\boldsymbol{\eta}_2 = \boldsymbol{0}$ represents the flux of the likelihood that the C molecule with the second-smallest $||\boldsymbol{\eta}_2||$ value diffuses over the sphere of radius r_2 set by the currently closest C molecule. In other words, it accounts for the fact that the molecule of C that is the second-closest to the origin can diffuse inwards and become the closest molecule to the origin.

In the bimolecular case considered by Smoluchowski, the probability density relates to the likelihood of finding any molecule of B at a particular position, while in the trimolecular case we have been careful to restrict our attention to the state associated with the closest molecule of C. This disparity arises because we have assumed that our trimolecular reaction boundary $\partial\Omega_R$ extends a very small distance, at most $\sigma_{\max}$, in the $\boldsymbol{\eta}_1$ direction, but may be comparatively long in the $\boldsymbol{\eta}_2$ direction. In the extreme case where $f(r_2) = \sigma_{\max}$ any molecule of C will satisfy the reaction condition regardless of its proximity to A and B once $r_1 = \sigma_{\max}$, and we must specify a particular molecule of C to be involved in the reaction to avoid ambiguity. Moreover, particle-based simulations of reaction-diffusion systems often update the position of molecules using finite time steps [64–66] which means that molecules are moved using small discrete displacements rather than continuously. If a pair of A and B molecules is such that their separation r_1

is just larger than $f(r_2)$ they can 'jump' through the reaction boundary during the next time step, so that $r_1 < f(r_2)$ following the position updates. At this point, there can again be multiple molecules of C close enough to satisfy the reaction condition, even if f is not constant. In theory, the same problem exists when simulating bimolecular reactions and the distribution for the closest molecule to Smoluchowski's reaction boundary can be derived analytically [52]. However, in practice σ is small enough that the likelihood that two molecules of B are close enough to A to react at any given moment is insignificant. Thus, unlike the trimolecular case, it is always clear which molecule of B should react with a particular molecule of A.

To determine a unique solution for $P(\boldsymbol{\eta}, t | \boldsymbol{Z}_2)$ we require appropriate initial and boundary conditions. To this end we assume that initially all the molecules are distributed uniformly at random throughout Ω so that the initial condition is given by the boundary-free steady-state solution of Equation (II.19)

$$P(\boldsymbol{\eta}, 0 | \boldsymbol{Z}_2) = \frac{c}{V} \exp\left(\frac{-4\pi c r_2^3}{3}\right). \tag{II.20}$$

Moreover, we know that the system will be absorbed when the state associated with the closest molecule of C crosses $\partial \Omega_R$, which leads to the inner boundary condition

$$P(\boldsymbol{\eta} \in \partial \Omega_R, t | \boldsymbol{Z}_2) = 0. \tag{II.21}$$

Notice that this condition reduces to Equation (II.6) when the domain contains only a single molecule of C. Infinitely far from $\partial \Omega_R$ in both the $\boldsymbol{\eta}_1$ and $\boldsymbol{\eta}_2$ direction, the probability density is unperturbed by the absorption of states on $\partial \Omega_R$ so that

$$\lim_{r_1 \to \infty} P(\boldsymbol{\eta}, t | \boldsymbol{Z}_2) = \frac{c}{V} \exp\left(\frac{-4\pi c r_2^3}{3}\right) \quad \text{and} \tag{II.22a}$$

$$\lim_{r_2 \to \infty} P(\boldsymbol{\eta}, t | \boldsymbol{Z}_2) = \lim_{r_2 \to \infty} \frac{c}{V} \exp\left(\frac{-4\pi c r_2^3}{3}\right) = 0. \tag{II.22b}$$

Finally, the flux of the probability density in the $\boldsymbol{\eta}_2$ direction should vanish at $r_2 = 0$ which amounts to requiring that

$$\frac{\partial P(\boldsymbol{\eta}, t | \boldsymbol{Z}_2)}{\partial r_2} = 0 \quad \text{at } r_2 = 0. \tag{II.23}$$

Equation (II.19), subject to the conditions in Equations (II.20)–(II.23), describes the evolution of the state that will cause the system to be absorbed. However, solving this PDE when $\partial \Omega_R$ is chosen arbitrarily is very difficult. If $\partial \Omega_R$ extends a small distance in both r_1 and r_2 (rather than just in r_1 as assumed in Equation (II.5)) then the advection term in Equation (II.19) becomes negligible, and the problem reduces to the trimolecular generalisation of Smoluchowski's reaction condition considered by Flegg [51], for which an exact solution can be found. Outside of this regime, we are not aware of an exact solution, but it is possible to construct a leading-order solution using singular perturbation methods.

Similar to the bimolecular case considered by Smoluchowski, the full time-dependent solution of Equation (II.19) will rapidly converge to a steady state, since $\partial \Omega_R$ only extends a small distance in the $\boldsymbol{\eta}_1$ direction [47]. Thus, we will focus on computing the steady-state solution of the PDE, which will be radially symmetric in both $\boldsymbol{\eta}_1$ and $\boldsymbol{\eta}_2$ because the boundary conditions (Equations (II.20)–(II.23)) only depend on the corresponding radial coordinates r_1 and r_2. That is, the steady-state solution of Equation (II.19), which we will denote $P(r_1, r_2)$ henceforth, will only depend on r_1 and r_2.

In the limit that $\sigma_{\max} \to 0$, $\partial \Omega_R$ becomes a sphere of radius 0 and, in effect, the absorbing boundary vanishes. In this case, the steady-state solution to Equation (II.19) is the initial condition from Equation (II.20). However, this solution has no r_1 dependence and so will never satisfy the boundary condition on $\partial \Omega_R$ for any finite value of $\sigma_{\max}$. This behaviour indicates that there exists a boundary layer [67] near $\partial \Omega_R$. That is, in the vicinity of the inner boundary, we expect the steady-state solution to change rapidly from the boundary-free steady-state solution to one that satisfies the boundary condition.

In Appendix B we perform a perturbation expansion of $P(r_1, r_2)$ near $\partial \Omega_R$ and apply standard singular perturbation techniques to derive the leading-order term

$$P_0(r_1, r_2) = \frac{c}{V} \exp\left(\frac{-4\pi c r_2^3}{3}\right)\left(1 - \frac{f(r_2)}{r_1}\right), \tag{II.24}$$

which serves as the leading-order approximation to P in that it neglects corrections of $O(\sigma_{\max}^2)$. We henceforth refer to P_0 as the leading-order solution.

The leading-order solution can be used to approximate the steady-state reaction rate, which is the total flux of $P(r_1, r_2)$ over $\partial\Omega_R$. The outward facing unit normal vector to $\partial\Omega_R$ is

$$\hat{\boldsymbol{n}}_{\text{out}} = -\left(1 + \left(\sigma_{\max}\frac{dF(r_2)}{dr_2}\right)^2\right)^{-\frac{1}{2}}\left(\hat{\boldsymbol{r}}_1 - \sigma_{\max}\frac{dF(r_2)}{dr_2}\hat{\boldsymbol{r}}_2\right), \tag{II.25}$$

hence, to first order in $\sigma_{\max}$, only the diffusive flux in the $\hat{\boldsymbol{r}}_1$ direction contributes. That is, the steady-state reaction rate can be approximated by

$$K_1(c) = \int_0^\infty \left(\hat{D}_1 \frac{\partial P(r_1, r_2)}{\partial r_1}\hat{\boldsymbol{r}}_1 \cdot 4\pi(f(r_2))^2\hat{\boldsymbol{r}}_1\right)4\pi r_2^2\,dr_2, \tag{II.26}$$

which can be simplified to

$$K_1(c) = \int_0^\infty \frac{4\pi\hat{D}_1 f(r_2)}{V}c\exp\left(\frac{-4\pi cr_2^3}{3}\right)4\pi r_2^2\,dr_2, \tag{II.27}$$

using Equation (II.24) and neglecting the $O(\sigma_{\max}^2)$ terms.

Equation (II.27) matches the expression used by Kearney and Flegg [50] to determine the function $f(r_2)$, which defines the boundary $\partial\Omega_R$ required to reproduce a given reaction rate $K_1(c)$. However, to arrive at this expression, several contributions to the flux across $\partial\Omega_R$ must be ignored. Firstly, there is an $O(\sigma_{\max}^2)$ correction to the leading-order solution and hence to the diffusive flux in the $\hat{\boldsymbol{r}}_1$ direction. In addition, there is an $O(\sigma_{\max}^2)$ contribution to the flux that arises from the diffusive and advective fluxes in the $\hat{\boldsymbol{r}}_2$ direction. Neglecting these contributions means that the functional form derived for $\partial\Omega_R$ will not be exact, resulting in small errors in the reaction rate reproduced by particle-based simulations that use this reaction boundary. Although these errors were known to Kearney and Flegg [50], they did not examine them in detail because it was difficult to isolate them from other sources of error present in their simulations.

Ideally, we would quantify these corrections analytically by continuing our singular perturbation analysis. However, as shown in Appendix B, standard techniques are not sufficient to derive the $O(\sigma_{\max}^2)$ term in the perturbation expansion of $P(r_1, r_2)$. Therefore, to quantify the expected $O(\sigma_{\max}^2)$ corrections, we seek a finite element solution to the problem that can be compared to the leading-order solution in Equation (II.24).

III.   MIXED-PRIMAL FORMULATION

The quantity of primary concern for particle-based simulations is the steady-state reaction rate, which corresponds to the flux of $P(r_1, r_2)$ over the reaction boundary $\partial\Omega_R$. One approach to compute this flux is to use a reconstruction from the finite element solution to the original form of the PDE in Equation (II.19) (see, e.g., [68]), but we opt for using a mixed-primal reformulation of the problem (which might be more appropriate to preserve the divergence structure [69]), and solve for the flux

$$\boldsymbol{s}(r_1, r_2) = -\left(\nabla P(r_1, r_2) + \frac{r_2^2 P(r_1, r_2)^2}{Q(r_1, r_2)}\hat{\mathbf{r}}_2\right), \tag{III.1}$$

directly, where

$$\nabla P(r_1, r_2) = \frac{\partial P(r_1, r_2)}{\partial r_1}\hat{\mathbf{r}}_1 + \frac{\partial P(r_1, r_2)}{\partial r_2}\hat{\mathbf{r}}_2. \tag{III.2}$$

Notice that we have introduced the *density moment*

$$Q(r_1, r_2) = \int_{r_2}^\infty P(r_1, r_2')r_2'^2\,dr_2', \tag{III.3}$$

which enables us to avoid directly calculating the integral in the Equation (II.19). The steady-state is now governed by a coupled system of PDEs

$$\boldsymbol{s}(r_1, r_2) + \left(\nabla P(r_1, r_2) + \frac{r_2^2 P(r_1, r_2)^2}{Q(r_1, r_2)}\hat{\mathbf{r}}_2\right) = 0, \tag{III.4a}$$

$$\nabla \cdot (D\boldsymbol{s}(r_1, r_2)) = 0, \quad \text{and} \tag{III.4b}$$

$$\frac{\partial Q(r_1, r_2)}{\partial r_2} + r_2^2 P(r_1, r_2) = 0, \tag{III.4c}$$

where D is a matrix of the diffusion coefficients such that,

$$D = \begin{bmatrix} \hat{D}_1 & 0 \\ 0 & \hat{D}_2 \end{bmatrix}, \tag{III.5}$$

and $\nabla \cdot \boldsymbol{s}(r_1, r_2)$ denotes the radial divergence of $\boldsymbol{s}(r_1, r_2)$, that is,

$$\nabla \cdot \boldsymbol{s}(r_1, r_2) = \frac{1}{r_1^2} \frac{\partial}{\partial r_1} \left(r_1^2 \boldsymbol{s}(r_1, r_2) \cdot \hat{\boldsymbol{r}}_1 \right) + \frac{1}{r_2^2} \frac{\partial}{\partial r_2} \left(r_2^2 \boldsymbol{s}(r_1, r_2) \cdot \hat{\boldsymbol{r}}_2 \right). \tag{III.6}$$

The corresponding steady-state reaction rate can be computed straightforwardly by evaluating

$$K(c) = \int_0^\infty D\boldsymbol{s}(r_1, r_2) \cdot \hat{\boldsymbol{n}}_{\text{out}} (4\pi f(r_2) r_2)^2 \, \mathrm{d}r_2, \tag{III.7}$$

where we recall that $\hat{\boldsymbol{n}}_{\text{out}}$ is the outward facing unit normal vector to $\partial\Omega_R$.

In principle the boundary conditions for $P(r_1, r_2)$ remain unchanged except that the no-flux condition defined in Equation (II.23) now defines a boundary condition on $\boldsymbol{s}(r_1, r_2)$

$$\boldsymbol{s}(r_1, r_2) \cdot \hat{\boldsymbol{r}}_2 = 0 \quad \text{at } r_2 = 0. \tag{III.8}$$

However, we have assumed that the domain Ω is very large (effectively infinite) in defining these conditions, and representing such a large domain inherently limits the resolution of the finite element mesh. This is problematic because we must be able to resolve the rapid change in the solution expected within the boundary layer near $\partial\Omega_R$. Therefore, it is necessary to consider a domain amenable for the finite element discretisation

$$\Omega_{\text{FE}} = \{(r_1, r_2) : f(r_2) \le r_1 \le r_1^{\max}, 0 \le r_2 \le r_2^{\max}\}, \tag{III.9}$$

that is not necessarily sufficiently large for these boundary conditions to be valid. The inner boundary condition from Equation (II.20) transfers trivially to Ω_{FE},

$$P(r_1, r_2) = 0 \quad \text{on } r_1 = f(r_2), \tag{III.10}$$

but the remaining conditions in Equations (II.22a) and (II.22b) require more careful consideration.

We expect the leading-order contribution to $P(r_1, r_2)$ to decay exponentially as r_2 increases. The rate of decay is expected to match that of the value on the boundary, given in Equation (II.22b), and so the value imposed at $r_2 = r_2^{\max}$ very quickly approaches zero. Therefore, the error that arises from imposing

$$P(r_1, r_2) = \frac{c}{V} \exp\left(\frac{-4\pi c r_2^3}{3} \right) \quad \text{at } r_2 = r_2^{\max}, \tag{III.11}$$

for finite $r_2^{\max}$, very quickly approaches zero as $r_2^{\max}$ is increased. Adopting this condition implies that we must also have

$$Q(r_1, r_2) = \frac{1}{4\pi V} \exp\left(\frac{-4\pi c r_2^3}{3} \right) \quad \text{at } r_2 = r_2^{\max}. \tag{III.12}$$

In contrast, as r_1 increases, we expect the leading-order solution to decay to the boundary condition in Equation (II.22a) with the reciprocal of r_1. That is, we expect the solution to converge to the outer solution much more slowly in the $\hat{\boldsymbol{r}}_1$ direction than in the $\hat{\boldsymbol{r}}_2$ direction and require $r_1^{\max}$ to be significantly larger than $r_2^{\max}$ for the boundary condition to be correct. Even if $r_1^{\max}$ is $O(1/\sigma_{\max})$ adopting the boundary condition in Equation (II.22a) incurs an $O(\sigma_{\max}^2)$ error that arises from the $O(\sigma_{\max})$ contribution to $P(r_1, r_2)$. To avoid introducing this unnecessary error we use the leading-order solution to modify the boundary condition for finite $r_1^{\max}$ and instead impose,

$$P(r_1, r_2) = \frac{c}{V} \exp\left(\frac{-4\pi c r_2^3}{3} \right) \left(1 - \frac{f(r_2)}{r_1} \right) \quad \text{at } r_1 = r_1^{\max}. \tag{III.13}$$

This boundary condition neglects any $O(\sigma_{\max}^2)$ corrections to the solution; however, we expect these corrections to decay polynomially with increasing r_1 similar to the $O(\sigma_{\max})$ term in the leading-order solution. Therefore, the error introduced by adopting this condition can be made negligible by making $r_1^{\max}$ sufficiently large.

The finite element formulation of Equation (III.4) along with convergence testing for the adopted scheme is provided in Appendix C.

IV. RESULTS

To examine the accuracy of the leading-order solution in Equation (II.24) in this section we compare it to the finite element solution of Equation (III.4), which is the mixed-primal reformulation of the steady-state version of the original PDE in Equation (II.19). For this comparison the reaction boundary is

$$\partial\Omega_R = \left\{ (\boldsymbol{\eta}_1, \boldsymbol{\eta}_2) : r_1 = \sigma_{\max}\exp\left(\frac{-4\pi\Gamma r_2^3}{3}\right) \right\}, \tag{IV.1}$$

where $\Gamma > 0$ is a parameter that controls the rate at which the height of the boundary decays as r_2 increases, and the finite element solution is computed over the domain

$$\Omega_{\mathrm{FE}} = \left\{ (r_1, r_2) : \sigma_{\max}\exp\left(\frac{-4\pi\Gamma r_2^3}{3}\right) \leq r_1 \leq 5, 0 \leq r_2 \leq 5 \right\}. \tag{IV.2}$$

Using Equation (II.27) we find that the steady-state reaction rate for this domain can be approximated by

$$K_1(c) = \frac{4\pi\hat{D}_1\sigma_{\max}c}{V_{\mathrm{FE}}(c+\Gamma)}, \tag{IV.3}$$

where $V_{\mathrm{FE}} = (4/3)\pi(r_1^{\max})^3$ and we have implicitly adopted the limit $r_2^{\max} \to \infty$ which introduces a negligible error compared to integrating up until $r_2^{\max} = 5$. In Subsection IV A we examine the steady-state finite element solution for this particular choice of $\partial\Omega_R$ and compare the corresponding reaction rate with Equation (IV.3). Then in Subsection IV B we demonstrate how to alter $\partial\Omega_R$ so that the observed reaction rate better replicates the desired reaction rate. In other words, we show how to correct for the errors incurred when adopting the approximation in Equation (IV.3).

The reaction boundary defined in Equation (IV.1) is of particular interest because it was used by Kearney and Flegg [50] in their particle-based simulation of the system we are considering. Although Kearney and Flegg briefly compared the reaction rate obtained from their simulation to $K_1(c)$, their results contained additional sources of error beyond those introduced by the approximation itself, making it impossible to isolate these contributions. In contrast, the finite element solution presented here is free from such confounding factors, making it possible to isolate the higher-order corrections to steady-state reaction rate.

Before proceeding we note that all quantities in this article are assumed to be dimensionless. Lengths are nondimensionalised with respect to a characteristic length scale, chosen such that the length of the domain is $r_1^{\max} = r_2^{\max} = 5$. Therefore, any concentrations stated denote the number of particles per unit of dimensionless volume V_{FE}. Unless otherwise stated all molecules are assumed to diffuse at equal dimensional rates, and a characteristic time scale is chosen such that the dimensionless diffusion coefficients of species A, B and C are all equal to one. The corresponding dimensionless diffusion coefficients for $\boldsymbol{\eta}_1$ and $\boldsymbol{\eta}_2$ are $\hat{D}_1 = 2$ and $\hat{D}_2 = 1.5$, respectively.

A. Comparison of finite element and leading-order solutions

To isolate the $O(\sigma_{\max}^2)$ corrections to the leading-order solution P_0, we consider the (scaled) difference $\delta P(r_1, r_2)$ between the finite element approximation of the density $P(r_1, r_2)$, which we denote by $P_h(r_1, r_2)$, and Equation (II.24)

$$\delta P(r_1, r_2) = 4\pi r_2^2\left(P_h(r_1, r_2) - \frac{c}{V_{\mathrm{FE}}}\exp\left(\frac{-4\pi c r_2^3}{3}\right)\left(1 - \frac{\sigma_{\max}}{r_1}\exp\left(\frac{-4\pi\Gamma r_2^3}{3}\right)\right) \right). \tag{IV.4}$$

The factor of $4\pi r_2^2$ is included since it is more convenient to work with the scaled probability density $4\pi r_2^2 P(r_1, r_2)$, which represents the probability to find the closest molecule of C on the surface of a sphere of radius r_2 that is centred on the origin. Figure IV.1 depicts δP in the case that $\sigma_{\max} = 0.1$ and $\Gamma = 1$, while we set $c = 10$ because it results in a sufficiently concentrated density profile for the associated flux to be easily visible near $\partial\Omega_R$; see Figure IV.2. The surface plot in Figure IV.1a displays the entirety of Ω_{FE} while Figure IV.1b displays a subdomain that only extends to $r_1 = 0.5$ and $r_2 = 1$.

As expected, the solutions differ the most near $\partial\Omega_R$ while the difference decays as both r_1 and r_2 increase. Notice that while δP decays very rapidly to zero as r_2 increases, it decays much more slowly as r_1 increases and remains finite even very close to the boundary at $r_1 = r_1^{\max}$; δP vanishes on this boundary since we enforce equality between the solutions there. This suggests that, similar to the $O(\sigma_{\max})$ contribution present in Equation (II.24), the $O(\sigma_{\max}^2)$ contributions to the solution decay exponentially as r_2 increases, but polynomially as r_1 increases. Moreover, we can see that P_0 underestimates the probability, resulting in the yellow region where $\delta P(r_1, r_2) > 0$, that the closest molecule is
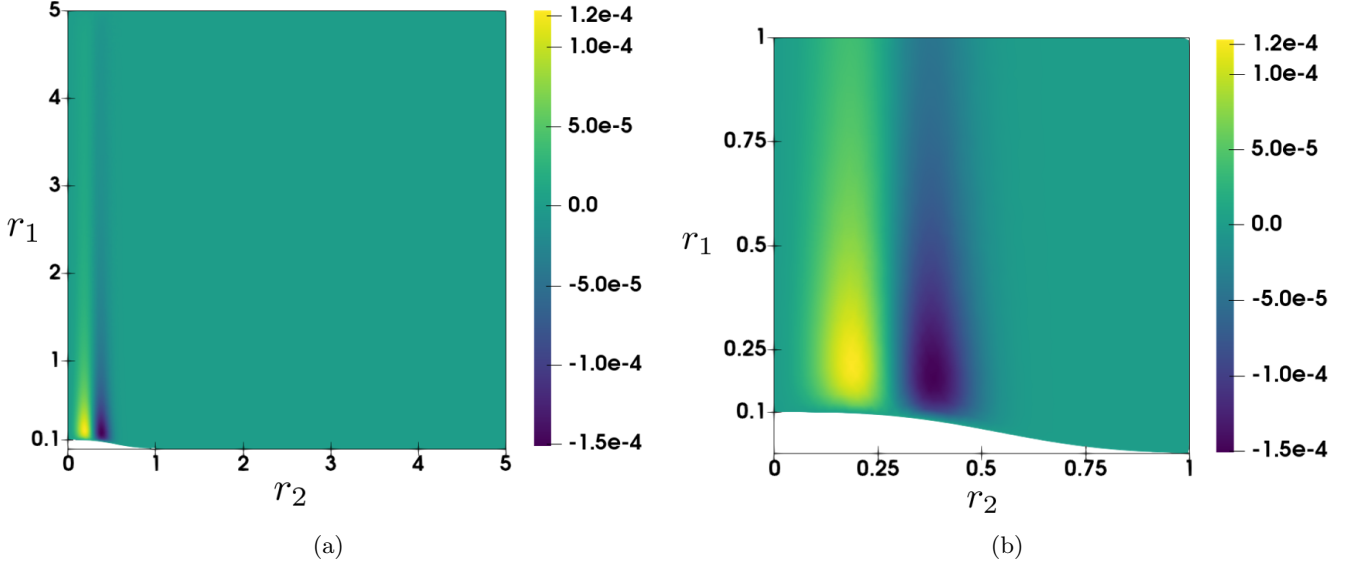
(a)

(b)

FIG. IV.1: The (scaled) difference $\delta P\left(r_1, r_2\right)$, defined in Equation (IV.4), between the steady-state finite element solution $P_h\left(r_1, r_2\right)$ and the leading-order solution $P_0(r_1, r_2)$ for $\hat{D}_1 = 2$, $\hat{D}_2 = 1.5$, $\sigma_{\max} = 0.1$, $\Gamma = 1$, and $c = 10$. The leading-order solution underestimates the probability, resulting in the yellow region where $\delta P\left(r_1, r_2\right) > 0$, that the closest molecule of C is near to the origin and instead favours larger values of r_2, which results in the dark blue region where $\delta P\left(r_1, r_2\right) < 0$. This discrepancy arises because P_0 neglects the advection towards the origin in the $\hat{\boldsymbol{r}}_2$ (horizontal) direction. The difference appears most pronounced near the bottom boundary $\partial\Omega_R$, defined in Equation (IV.1), but this is because the solutions decay with increasing r_1. The surface plot in (a) shows the finite element domain from Equation (IV.2), while the plot in (b) shows the subdomain
$$\left\{(r_1, r_2) : \sigma_{\max}\exp\left(\frac{-4\pi\Gamma r_2^3}{3}\right) \le r_1 \le 1, 0 \le r_2 \le 1\right\}.$$

close to the origin and instead favours larger values of r_2, resulting in the dark blue region where $\delta P\left(r_1, r_2\right) < 0$. This is because the leading-order solution results from considering the limit $\sigma_{\max}^2 \to 0$ in Equation (B.2), which amounts to ignoring both the diffusive motion in the $\hat{\boldsymbol{r}}_2$ direction and, more severely, the advective motion towards the origin in this direction.

Similarly, when approximating the steady-state reaction rate using $K_1(c)$ from Equation (II.27), we only consider the $O(\sigma_{\max})$ contributions to the flux of the probability density over $\partial\Omega_R$. This effectively ignores the contribution to this reaction rate from the flux in the $\hat{\boldsymbol{r}}_2$ direction as well as an $O(\sigma_{\max}^2)$ correction to the contribution in the $\hat{\boldsymbol{r}}_1$ direction, which arises from the correction of the same order to P_0. The (scaled) $O(\sigma_{\max}^2)$ correction to the diffusive flux in the $\hat{\boldsymbol{r}}_1$ direction is calculated using the finite element approximation to the full flux $\boldsymbol{s}\left(r_1, r_2\right)$, which we denote by $\boldsymbol{s}_h\left(r_1, r_2\right)$,

$$\delta s_1(r_1, r_2) = 4\pi r_2^2\hat{D}_1\left(\boldsymbol{s}_h\left(r_1, r_2\right) \cdot \hat{\boldsymbol{r}}_1 + \nabla P_0(r_1, r_2) \cdot \hat{\boldsymbol{r}}_1\right), \tag{IV.5}$$

and is shown in Figure IV.2a, where in this case

$$\nabla P_0(r_1, r_2) \cdot \hat{\boldsymbol{r}}_1 = \frac{c\sigma_{\max}}{V_{\mathrm{FE}}r_1^2}\exp\left(\frac{-4\pi(c + \Gamma)r_2^3}{3}\right). \tag{IV.6}$$

Since $K_1(c)$ ignores the flux in the $\hat{\boldsymbol{r}}_2$ direction entirely, the (scaled) $O(\sigma_{\max}^2)$ correction to this component is simply the total flux in this direction

$$\delta s_2(r_1, r_2) = 4\pi r_2^2\hat{D}_2\boldsymbol{s}_h\left(r_1, r_2\right) \cdot \hat{\boldsymbol{r}}_2, \tag{IV.7}$$

and is shown in Figure IV.2b. In each case, we have restricted our attention to a subdomain of Ω_{FE} that only extends to $r_1 = 0.5$ and $r_2 = 1$, since the flux is negligible outside this subdomain. The behaviour of δs_1 mimics that of δP in that the flux of the leading-order solution underestimates the magnitude of the diffusive flux in the $\hat{\boldsymbol{r}}_1$ direction for small values of r_2, resulting in the dark blue region where $\delta s_1(r_1, r_2) < 0$, while overestimating it at larger values, resulting in the yellow region where $\delta s_1(r_1, r_2) > 0$. In addition, we can see that there will also be a correction in the

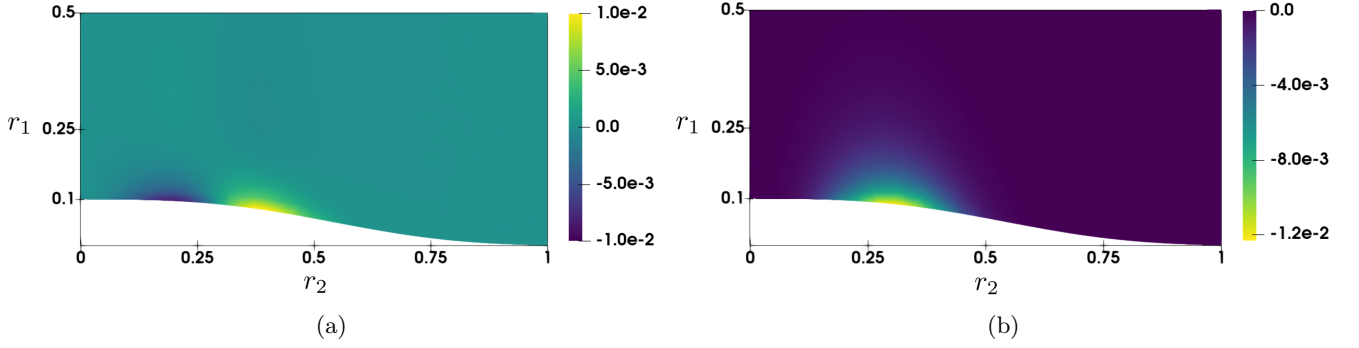(a)   (b)

FIG. IV.2: The corrections to the flux of the probability density that are neglected by the approximation $K_1(c)$ to the steady-state reaction rate defined in Equation (II.27), for $\hat{D}_1 = 2$, $\hat{D}_2 = 1.5$, $\sigma_{\max} = 0.1$, $\Gamma = 1$, and $c = 10$. The surface plot in (a) shows the (scaled) correction $\delta s_1(r_1, r_2)$ to the diffusive flux in the $\hat{\boldsymbol{r}}_1$ (vertical) direction defined by Equation (IV.5). The diffusive flux of the leading-order solution $P_0(r_1, r_2)$ underestimates the magnitude of the $\hat{\boldsymbol{r}}_1$ component of the finite element solution $\boldsymbol{s}_h(r_1, r_2)$ for values of r_2 less than approximately 0.25, resulting in the dark blue region where $\delta s_1(r_1, r_2) < 0$. In contrast, the magnitude of this flux is overestimated for larger values of r_2, resulting in the yellow region where $\delta s_1(r_1, r_2) > 0$. Similarly, the surface plot in (b) shows the (scaled) correction $\delta s_2(r_1, r_2)$ to the flux accounted for by $K_1(c)$ in the $\hat{\boldsymbol{r}}_2$ (horizontal) direction defined by Equation (IV.7). Since $K_1(c)$ entirely neglects the flux in this direction over $\partial \Omega_R$, as it is an $O(\sigma_{\max}^2)$ contribution, this correction is simply the $\hat{\boldsymbol{r}}_2$ component of the finite element solution $\boldsymbol{s}_h(r_1, r_2)$. Both plots display the subdomain
$$\{(r_1, r_2) : 0 \leq r_1 \leq 0.5, 0 \leq r_2 \leq 1\}.$$

same vicinity due to δs_2. Notice that both components of the flux point in the opposite direction to the respective radial unit vectors $\hat{\boldsymbol{r}}_1$ and $\hat{\boldsymbol{r}}_2$.

To better contextualise these corrections we now consider the total flux of P_h over $\partial \Omega_R$

$$K_{\mathrm{FE}}(c) = \int_0^{r_2^{\max}} D\boldsymbol{s}_h(r_1, r_2) \cdot \hat{\boldsymbol{n}}_{\mathrm{out}} (4\pi f(r_2) r_2)^2 \, \mathrm{d}r_2, \tag{IV.8}$$

which serves as a proxy for the exact reaction rate $K(c)$, although we will continue to use the subscript 'FE' to distinguish this approximate rate. We are concerned with how the corrections to the flux shown in Figure IV.2 affect this rate, and to quantify these contributions, we define three relative errors,

$$\delta K(c) = \frac{K_{\mathrm{FE}}(c) - K_1(c)}{K_1(c)}, \tag{IV.9a}$$

$$\delta K^1(c) = \frac{1}{K_1(c)} \left(\int_0^{r_2^{\max}} D\boldsymbol{s}_h(r_1, r_2) \cdot \hat{\boldsymbol{n}}_1 (4\pi f(r_2) r_2)^2 \, \mathrm{d}r_2 - K_1(c) \right), \tag{IV.9b}$$

and

$$\delta K^2(c) = \frac{1}{K_1(c)} \int_0^{r_2^{\max}} D\boldsymbol{s}_h(r_1, r_2) \cdot \hat{\boldsymbol{n}}_2 (4\pi f(r_2) r_2)^2 \, \mathrm{d}r_2, \tag{IV.9c}$$

where $\hat{\boldsymbol{n}}_i = (\hat{\boldsymbol{n}}_{\mathrm{out}} \cdot \hat{\boldsymbol{r}}_i)\hat{\boldsymbol{r}}_i$. Since $K_1(c)$ only considers the diffusive flux of P_0 over $\partial \Omega_R$ in the $\hat{\boldsymbol{r}}_1$ direction, $\delta K^1(c)$ essentially measures the relative error in the reaction rate that arises from neglecting $O(\sigma_{\max}^2)$ corrections to the flux of P in this direction. Similarly, $\delta K^2(c)$ measures the relative error that arises from neglecting the diffusive and advective flux of P over $\partial \Omega_R$ in the $\hat{\boldsymbol{r}}_2$ direction.

To explore how these errors behave as the shape of $\partial \Omega_R$ changes, we fix $c = 1$, $\hat{D}_1 = 2$, $\hat{D}_2 = 1.5$ and conduct two tests. In the first, we hold $\sigma_{\max} = 0.1$ constant and increase Γ from 0.25 to 3 in intervals of 0.25, while in the second we instead hold $\Gamma = 1$ constant and increase $\sigma_{\max}$ from 0.025 to 0.25 in intervals of 0.025.

The black, red and blue lines in Figure IV.3 depict the relative errors $\delta K(c)$, $\delta K^1(c)$ and $\delta K^2(c)$ respectively, in the case where $\sigma_{\max}$ is varied and Γ is held constant. In this case, $\delta K(c)$ and $\delta K^2(c)$ increase monotonically as $\sigma_{\max}$ increases, but $\delta K^1(c)$ only increases until $\sigma_{\max} = 0.225$ after which it begins to decrease. Moreover, at the same
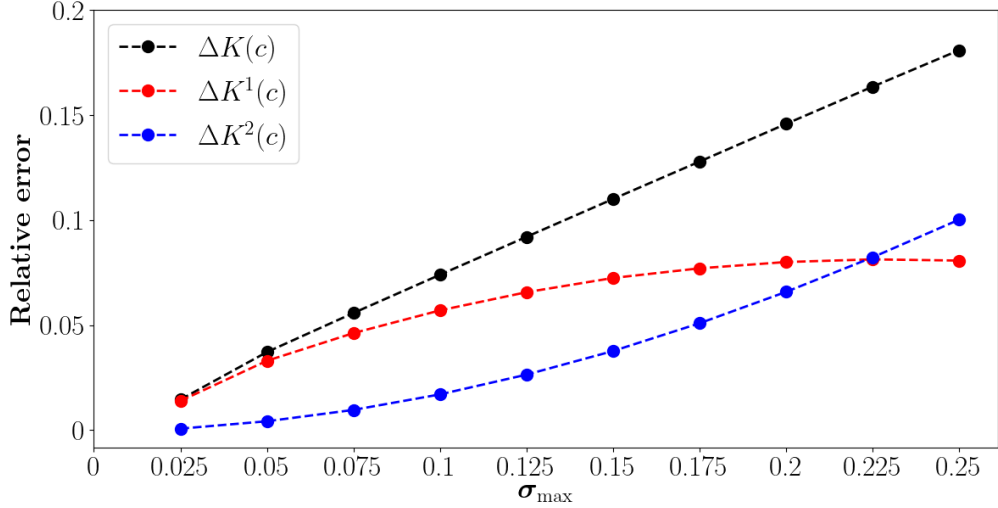
FIG. IV.3: The relative error between the steady-state reaction rate $K_{\text{FE}}(c)$ from Equation (IV.8), and the approximate reaction rate $K_1(c)$, given by Equation (II.27), calculated for $c = 1$, $\hat{D}_1 = 2$, $\hat{D}_2 = 1.5$, $\Gamma = 1$, while $\sigma_{\max}$ is increased from 0.025 to 0.25 in intervals of 0.025. The steady-state reaction rate is defined as the total flux of the probability density over the boundary $\partial\Omega_R$, defined by Equation (IV.1). The black line shows the total relative error $\delta K(c)$, defined in Equation (IV.9a), between $K_{\text{FE}}(c)$ and $K_1(c)$. This error arises because $K_1(c)$ neglects $O(\sigma_{\max}^2)$ contributions to the flux over $\partial\Omega_R$. Since there are contributions of this order over $\partial\Omega_R$ in both the $\hat{r}_1$ and $\hat{r}_2$ directions, we quantify them separately using the relative errors $\delta K^1(c)$ and $\delta K^2(c)$, defined in equations (IV.9b) and (IV.9c), and shown by the red, and blue lines respectively. That is, $\delta K^1(c)$ and $\delta K^2(c)$ represent the relative error that arises from ignoring $O(\sigma_{\max}^2)$ contributions to the flux over $\partial\Omega_R$ in the $\hat{r}_1$ and $\hat{r}_2$ directions respectively. The finite element solution used to calculate $K_{\text{FE}}(c)$ was evaluated over the domain
$$\Omega_{\text{FE}} = \left\{ (r_1, r_2) : \sigma_{\max}\exp\left(\frac{-4\pi\Gamma r_2^3}{3}\right) \leq r_1 \leq 5, 0 \leq r_2 \leq 5 \right\}.$$

point $\delta K^2(c)$ becomes greater than $\delta K^1(c)$ for the first time. This behaviour arises because the magnitude of the $\hat{r}_2$ component of the normal to the boundary, $\hat{n}_{\text{out}}$, increases with increasing $\sigma_{\max}$, while the magnitude of the $\hat{r}_1$ component decreases (see Equation (II.25)). Therefore, the flux over $\partial\Omega_R$ in the $\hat{r}_2$ direction increases, while the flux over this boundary in the $\hat{r}_1$ direction decreases. Finally, recalling that $K_1(c)$ is $O(\sigma_{\max})$, we note that $\delta K(c)$ growing linearly with $\sigma_{\max}$ indicates that the corrections to $K_1(c)$ are $O(\sigma_{\max}^2)$ as expected.

Similarly, Figure IV.4 displays the relative errors $\delta K(c)$, $\delta K^1(c)$ and $\delta K^2(c)$ as a black, red, and blue line, respectively, in the case where Γ is varied and $\sigma_{\max}$ is constant. The three relative errors increase monotonically, but the rate of increase appears to decrease as Γ increases. The height of $\partial\Omega_R$ decays more rapidly as Γ increases, but the relationship between this parameter and $\hat{n}_{\text{out}}$ is less straightforward. For any particular value of r_2, which defines a particular point on $\partial\Omega_R$, the magnitude of the $\hat{r}_2$ ($\hat{r}_1$) component of $\hat{n}_{\text{out}}$ will initially increase (decrease) with increasing Γ until it reaches a local maximum (minimum) after which it begins to decrease (increase) as Γ increases further. Moreover, the value of Γ at which this stationary point occurs decreases as r_2 increases. Therefore, for a fixed concentration and hence density profile, the approximation $\hat{n}_{\text{out}} = -\hat{r}_1$ initially becomes worse as Γ increases from zero and the relative errors all increase accordingly. However, if Γ continues to increase, eventually the magnitude of the $\hat{r}_2$ component of $\hat{n}_{\text{out}}$ in the region where the density is the most concentrated will begin to decay and $\hat{n}_{\text{out}}$ begins to converge to $-\hat{r}_1$ and so $K_{\text{FE}}(c)$ begins to converge to $K_1(c)$. Therefore, the relative errors will initially increase, plateau and eventually begin to decrease again once Γ becomes large enough.

B. Reaction boundary corrections

To reproduce realistic chemical kinetics, particle-based simulations must accurately reproduce known reaction rates. In other words, modellers typically begin with a desired reaction rate, which we denote $K_{\text{D}}(c)$, and then determine what reaction conditions should be imposed on the system to reproduce this rate. The expression for $K_1(c)$ given in Equation (II.27) is advantageous since it can be easily solved for the function $f(r_2)$, which defines $\partial\Omega_R$, via an inverse Laplace transform [50]. That is, it allows us to derive an analytic expression for the reaction boundary $\partial\Omega_R$
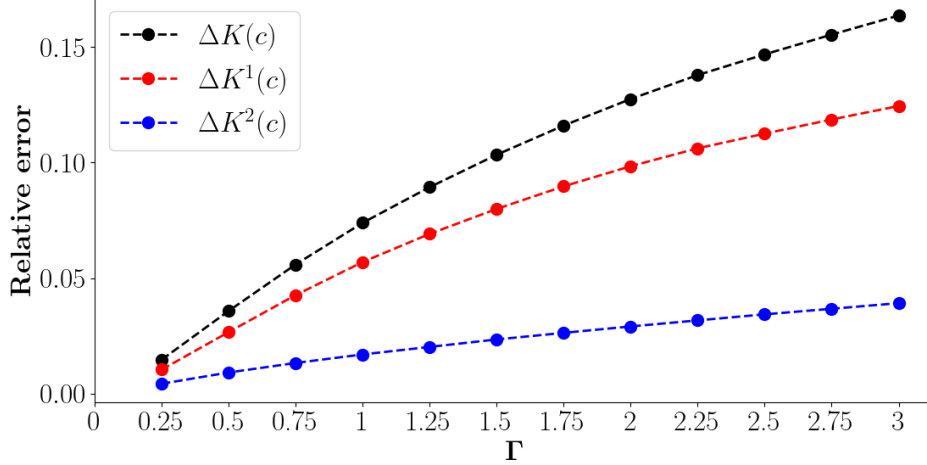
FIG. IV.4: The relative error between the steady-state reaction rate $K_{\mathrm{FE}}(c)$ from Equation (IV.8), and the approximate reaction rate $K_1(c)$, given by Equation (II.27), calculated for $c = 1$, $\hat{D}_1 = 2$, $\hat{D}_2 = 1.5$, and $\sigma_{\max} = 0.1$, while Γ is increased from 0.25 to 3 in intervals of 0.25. The steady-state reaction rate is defined as the total flux of the probability density over the boundary $\partial\Omega_R$, defined by Equation (IV.1). The black line shows the total relative error $\delta K(c)$, defined in Equation (IV.9a), between $K_{\mathrm{FE}}(c)$ and $K_1(c)$. This error arises because $K_1(c)$ neglects $O(\sigma_{\max}^2)$ contributions to the flux over $\partial\Omega_R$. Since there are contributions of this order over $\partial\Omega_R$ in both the $\hat{r}_1$ and $\hat{r}_2$ directions, we quantify them separately using the relative errors $\delta K^1(c)$ and $\delta K^2(c)$, defined in equations (IV.9b) and (IV.9c), and shown by the red, and blue lines respectively. That is, $\delta K^1(c)$ and $\delta K^2(c)$ represent the relative error that arises from ignoring $O(\sigma_{\max}^2)$ contributions to the flux over $\partial\Omega_R$ in the $\hat{r}_1$ and $\hat{r}_2$ directions respectively. The finite element solution used to calculate $K_{\mathrm{FE}}(c)$ was evaluated over the domain

$$\Omega_{\mathrm{FE}} = \left\{(r_1, r_2) : \sigma_{\max}\exp\left(\frac{-4\pi\Gamma r_2^3}{3}\right) \leq r_1 \leq 5, 0 \leq r_2 \leq 5\right\}.$$

that (approximately) matches a given rate $K_1(c)$. Thus, the obvious approach is to replace $K_1(c)$ with the desired rate $K_{\mathrm{D}}(c)$ and determine the corresponding reaction boundary. However, our results demonstrate that deriving $\partial\Omega_R$ in this way will result in a boundary that does not reproduce $K_{\mathrm{D}}(c)$ exactly. Instead, the simulated reaction rate (assuming that all other sources of error are negligible) will be given by Equation (III.7). This is problematic since small changes in the reaction rate can drastically change the behaviour of biochemical systems (for example, in systems that exhibit bistability and hysteresis [70, 71]) and, for the specific form of $\partial\Omega_R$ considered here, the relative error between $K_1(c)$—or in this case $K_{\mathrm{D}}(c)$—and $K_{\mathrm{FE}}(c)$ becomes large as $\sigma_{\max}$ or Γ increases. Therefore, we aim to adjust $\partial\Omega_R$ so that the reaction rate it produces—quantified by $K_{\mathrm{FE}}(c)$—more closely matches the desired rate $K_{\mathrm{D}}(c)$. Moreover, since during a simulation $\partial\Omega_R$ must be evaluated each time there is potential for a reaction to occur, we would like to retain an analytic expression for this boundary that is efficient to evaluate and seek to alter the parameters that define $\partial\Omega_R$ rather than its functional form. This amounts to assuming that the functional form of $K_{\mathrm{FE}}(c)$ is well approximated by that of $K_1(c)$.

To demonstrate how to correct $\partial\Omega_R$ in this manner we suppose that the desired reaction rate is given by

$$K_{\mathrm{D}}(c) = \frac{4\pi\hat{D}_1\sigma_{\mathrm{D}}c}{V_{\mathrm{FE}}(c + \Gamma_{\mathrm{D}})}, \tag{IV.10}$$

with $\sigma_{\mathrm{D}} = 0.1$ and $\Gamma_{\mathrm{D}} = 1$. Using Equation (II.27) we find that the boundary defined in Equation (IV.1) (approximately) matches this reaction rate. Therefore, we adopt this functional form for $\partial\Omega_R$ and set $\sigma_{\max} = 0.1$ and $\Gamma = 1$. In Figure IV.5 we compare $K_{\mathrm{D}}(c)$ and $K_{\mathrm{FE}}(c)$ for this initial boundary in the case that $\hat{D}_1 = 2$, $\hat{D}_2 = 1.5$ and c is increased from 1 to 20 in increments of 1. Figure IV.5a depicts $K_{\mathrm{D}}(c)$ and $K_{\mathrm{FE}}(c)$ using a blue line and the red points, respectively. The corresponding relative error,

$$\delta K_{\mathrm{FE}}(c) = \frac{K_{\mathrm{FE}}(c) - K_{\mathrm{D}}(c)}{K_{\mathrm{D}}(c)}, \tag{IV.11}$$

is shown in Figure IV.5b and decreases monotonically as c increases. This occurs because as c increases, the probability of finding the closest molecule of C close to the origin (at small r_2) increases and the probability density profile narrows,
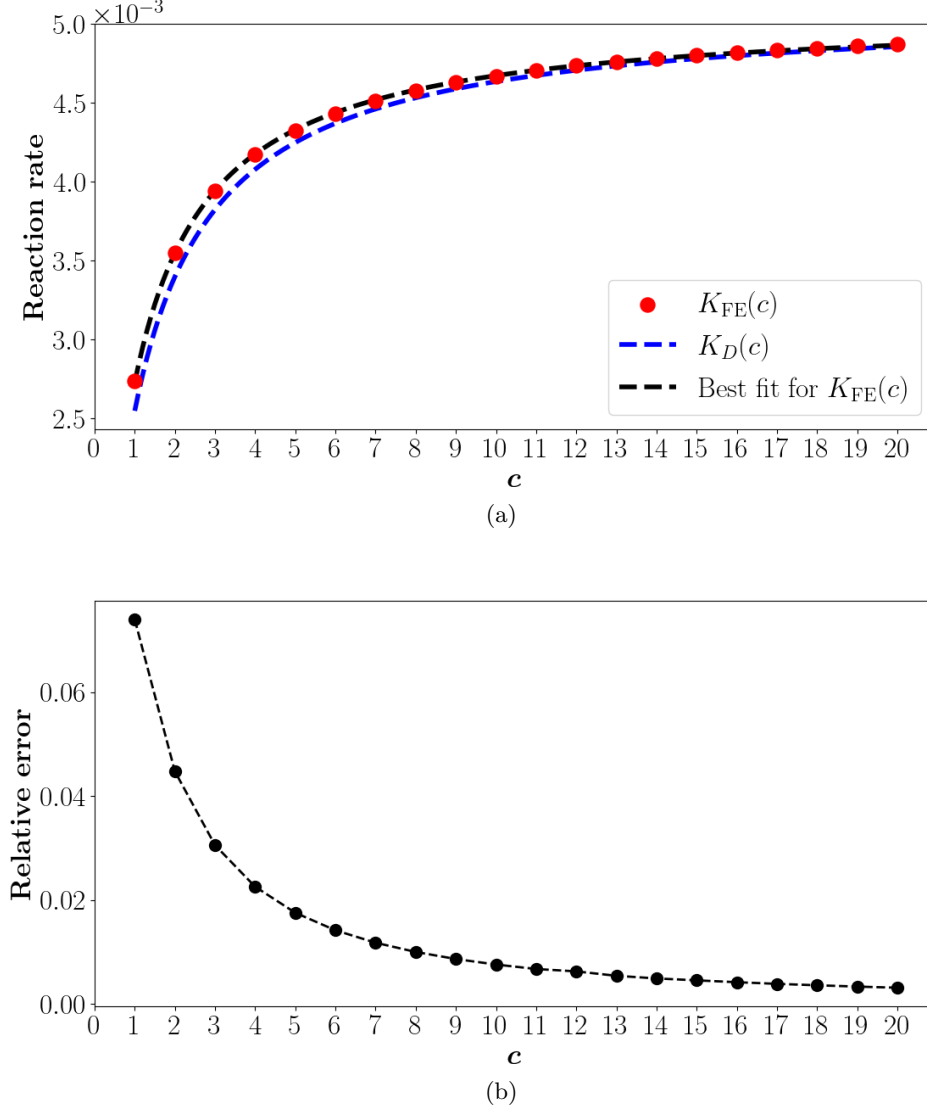
(a)

(b)

FIG. IV.5: The steady-state reaction rate $K_{\text{FE}}(c)$ obtained from the finite element solution via Equation (IV.8), for $\sigma_{\max} = 0.1$, $\Gamma = 1$, $\hat{D}_1 = 2$, and $\hat{D}_2 = 1.5$, while the concentration c is increased from 1 to 20 in increments of 1. The plot in (a) compares $K_{\text{FE}}(c)$, shown by the red points, to the desired reaction rate $K_{\text{D}}(c)$ shown by the blue line and defined in Equation (IV.10) with $\sigma_{\text{D}} = 0.1$ and $\Gamma_{\text{D}} = 1$. The black line shows the line of best fit for $K_{\text{FE}}(c)$ when assuming the model in Equation (IV.12) and is defined by the parameters $\sigma_{\text{E}} = 0.1$ and $\Gamma_{\text{E}} = 0.86$. The plot in (b) displays the relative error $\delta K_{\text{FE}}(c)$, defined in Equation (IV.11), between $K_{\text{FE}}(c)$ and $K_{\text{D}}(c)$ for the same set of parameters and shows that $\delta K_{\text{FE}}(c)$ decreases monotonically as c is increased.

which reduces the influence of the curvature of $\partial \Omega_R$ on the reaction rate. In other words, as P_h becomes more localised the relevant part of $\partial \Omega_R$ (in the region where $4\pi r_2^2 P(r_1, r_2) > 0$) is better approximated by a constant. This means that $K_{\text{FE}}(c)$ is well approximated by $K_1(c)$ and therefore matches $K_{\text{D}}(c)$ more closely since in this case $K_{\text{D}}(c) = K_1(c)$.

To better quantify the difference between $K_{\text{FE}}(c)$ and $K_{\text{D}}(c)$ across the range of concentrations considered we assume $K_{\text{FE}}(c)$ is well approximated by the functional form of $K_{\text{D}}(c)$, and fit the model

$$K_{\text{FE}}(c) = \frac{4\pi \hat{D}_1 \sigma_{\text{E}} c}{V_{\text{FE}}(c + \Gamma_{\text{E}})},\tag{IV.12}$$

to determine the 'effective' parameters σ_{E} and Γ_{E}. If $\partial \Omega_R$ reproduced the desired reaction rate exactly, then σ_{E} and Γ_{E} would be identical to σ_{D} and Γ_{D} respectively. However, we already know that this is not the case here and the

resulting line of best fit is defined by $\sigma_E = 0.1$ and $\Gamma_E = 0.86$ and is shown by the black dotted line in Figure IV.5a. Through this fit we can see that σ_D is well approximated by σ_E, but there is a large discrepancy between Γ_D and Γ_E with a corresponding relative error of 14%.

Our goal now is to alter $\partial\Omega_R$, by varying $\sigma_{\max}$ and Γ, so that the error between $K_{FE}(c)$ and $K_D(c)$ is minimised. It is important to emphasise that $K_D(c)$ is determined by the modeller, and that our goal is to determine a reaction boundary that reproduces this rate. In contrast, $K_1(c)$ and $K_{FE}(c)$ both approximate the reaction rate associated with the current reaction boundary $\partial\Omega_R$. The former does so through Equation (II.27), while the latter is connected to $\partial\Omega_R$ through Equation (IV.8) and serves as a proxy for the exact reaction rate $K(c)$. Crucially, altering $\partial\Omega_R$ changes $K_1(c)$ and $K_{FE}(c)$, but not $K_D(c)$.

Since the error between $K_D(c)$ and $K_{FE}(c)$ depends on the concentration, we use the Trust Region Reflective method developed by Branch *et al.* [72] to minimise the sum of squared residuals between these quantities. This method is available via the *least_squares* function in the open-source SciPy library [73]. We define the residual for a given concentration as

$$r(c) = K_{FE}(c) - K_D(c), \tag{IV.13}$$

and recall that initially $\sigma_{\max} = 0.1$ and $\Gamma = 1$ define $\partial\Omega_R$ through Equation (IV.1). In addition, we use Equation (IV.3) to derive an analytic approximation of the Jacobian for $K_{FE}(c)$. Each iteration of the algorithm we:

1. construct a finite element mesh $\mathcal{T}_h$ according to the current values of $\sigma_{\max}$ and Γ;

2. compute $K_{FE}(c)$, increasing c from 1 to 20 in intervals of size 1;

3. update the values of the parameters $\sigma_{\max}$ and Γ, thus defining the new boundary $\partial\Omega_R$ and Jacobian for the next iteration.

This process is continued until the sum of the squares of the residuals or the values of $\sigma_{\max}$ and Γ do not change significantly between successive iterations.

In our case, the optimisation yields $\sigma_{\max} = 0.10$ and $\Gamma = 1.19$ and we compare $K_{FE}(c)$ for this boundary to $K_D(c)$ in Figure IV.6. The blue line in Figure IV.6a represents $K_D(c)$, the red points denote $K_{FE}(c)$ calculated for the boundary in Equation (IV.1) defined by the optimised values of $\sigma_{\max}$ and Γ, and the black line is the line of best fit through these points for the model in Equation (IV.12). The new line of best fit is defined by $\sigma_E = 0.1$ and $\Gamma_E = 1.01$, which means that again σ_D is well approximated by σ_E, while the relative error between Γ_D and Γ_E has reduced in magnitude from 14% to just 1%. Similarly, Figure IV.6b shows a reduction in the relative error between $K_{FE}(c)$ and $K_D(c)$ for $c \leq 15$ while there is a slight increase in the error for $c > 15$. Finally, the sum of the squares of the residuals has been significantly reduced from 2.5×10^{-2} to 1.5×10^{-3}.

To demonstrate the effect of this correction in particle-based simulations, we use the algorithm developed by Kearney and Flegg [50] to simulate a system in which molecules of A, B and C react according to

$$\emptyset \xrightarrow{k_0} A \quad \text{and} \quad A + B + C \longrightarrow B + C, \tag{IV.14}$$
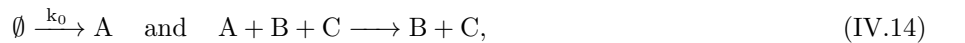
where k_0 is a zeroth-order rate constant that controls the production of A, and the trimolecular degradation of A is governed by the reaction boundary in Equation (IV.1).

The initial number of A molecules (N_A) is sampled from the corresponding steady-state distribution, which for this birth-death process is a Poisson distribution [74] with mean

$$E[N_A] = \frac{k_0 V_{PB}(c + \Gamma)}{4\pi \hat{D}_1 \sigma_{\max} bc}, \tag{IV.15}$$

where V_{PB} is the volume of the simulation domain. The number of B molecules (N_B) is chosen so that the concentration is $b = N_B/V_{PB} = 1$, while the number of C molecules is set to produce the desired concentration c. Setting $k_0 = 1/V_{PB}$ allows the trimolecular degradation of A to be computed as the inverse of $E[N_A]$, yielding the rate constant

$$k_{PB}(c) = \frac{1}{E[A]} = \frac{4\pi \hat{D}_1 \sigma_{\max} c}{c + \Gamma}, \tag{IV.16}$$

which is related the the corresponding reaction rate by $K_{PB}(c) = k_{PB}(c)/V_{PB}$.

Notice that we have assumed that the volume of the particle-based simulation domain differs from V_{FE}. This is convenient because it allows us to assume that V_{PB} is an integer—we consider $V_{PB} = 50$ here—which is helpful when setting reactant concentrations. Moreover, while V_{FE} must be large enough for the boundary conditions in
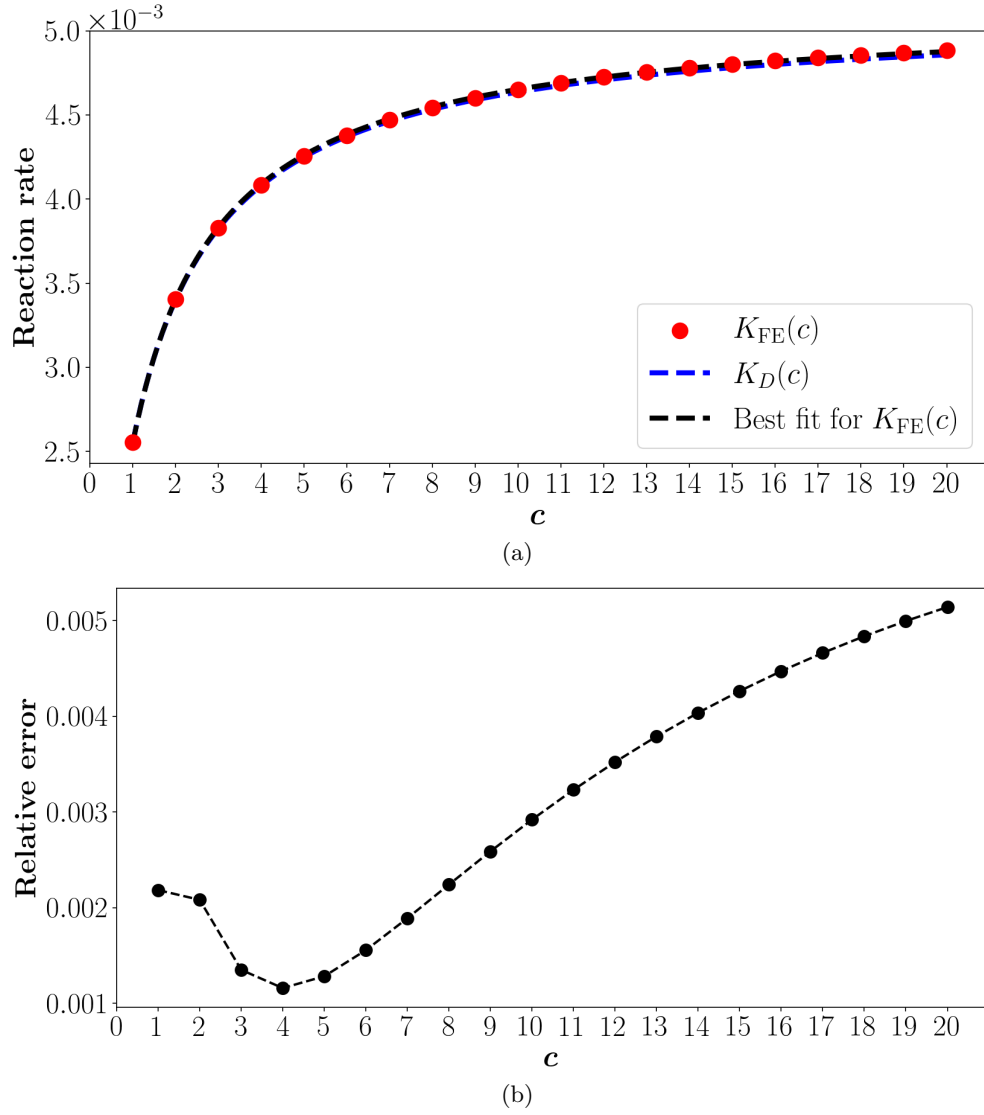
(a)

(b)

FIG. IV.6: The steady-state reaction rate $K_{\text{FE}}(c)$, computed via Equation (IV.8) using the corrected boundary defined by Equation (IV.1) with $\sigma_{\max} = 0.1$ and $\Gamma = 1.19$. We consider $\hat{D}_1 = 2$, $\hat{D}_2 = 1.5$, and $c = 1$ to 20 in steps of 1 to match Figure IV.5. In (a) $K_{\text{FE}}(c)$, shown by the red points, is compared to the desired reaction rate $K_{\text{D}}(c)$, shown by the blue line, and defined in Equation (IV.10) with $\sigma_{\text{D}} = 0.1$ and $\Gamma_{\text{D}} = 1$. The black line shows the line of best fit for $K_{\text{FE}}(c)$ assuming the model in Equation (IV.12) and is defined by the parameters $\sigma_{\text{E}} = 0.1$ and $\Gamma_{\text{E}} = 1.01$. The plot in (b) displays the corresponding relative error $\delta K_{\text{FE}}(c)$, defined in Equation (IV.11), between $K_{\text{FE}}(c)$ and $K_{\text{D}}(c)$. Compared to Figure IV.5b we can see that the corrected boundary reduces the relative error for $c \leq 15$. However, now the relative error tends to increase with increasing c and is worse than it was previously for $c > 15$.

Equations (III.11)–(III.13) to be valid, no such constraint applies to V_{PB}. Instead, because we impose periodic boundary conditions on the domain, V_{PB} only needs to be large enough to contain a sufficient number of C molecules for the probability density $P(r_1, r_2)$, which was derived in the limit that $N_C \to \infty$ (see Equation (II.13)), to serve as a good approximation for the distribution of the closest molecule of C to the centre of diffusion of any pair of A and B molecules. Tests conducted by Kearney and Flegg [50] indicate that $N_C \geq 50$ is sufficient.

All molecules are initially distributed uniformly at random throughout the simulation domain, and any molecule of A produced by the zeroth-order reaction also has its initial position chosen uniformly at random. The diffusion coefficients remain equal to one for A and B, but we increase the diffusion constant of C to $D_2 = 5$, so that $\hat{D}_2 = 5.5$. This increases the flux in the $\boldsymbol{\eta}_2$ direction and hence the magnitude of the error, allowing the correction to be resolved with fewer simulation replicates. However, this change only slightly alters the parameters for the corrected boundary,

which is now defined by $\sigma_{\max} = 0.099$ and $\Gamma = 1.20$. Dimensionless time steps of $t_{\text{step}} = 10^{-6}$ are used to update the positions of the molecules, and the simulation is run until $t = 20$, after which the value of N_A is sampled. For each value of $c \in \{1, 2, 4\}$ we perform 10^4, 10^4 and 1.5×10^4 replicates, respectively, and calculate $k_{\text{PB}}(c)$ according to Equation (IV.16).

The results for both the original uncorrected reaction boundary ($\sigma_{\max} = 0.1$ and $\Gamma = 1$) and the corrected reaction boundary ($\sigma_{\max} = 0.099$ and $\Gamma = 1.20$) are shown in Table IV.1. To compare $k_{\text{PB}}(c)$ to the desired reaction rate $K_{\text{D}}(c)$, with $\sigma_{\text{D}} = 0.1$ and $\Gamma_{\text{D}} = 1$, we calculate the relative error

$$\delta k_{\text{PB}}(c) = \frac{k_{\text{PB}}(c) - V_{\text{FE}} K_{\text{D}}(c)}{V_{\text{FE}} K_{\text{D}}(c)}, \tag{IV.17}$$

which we then compare to the corresponding relative error, $\delta K_{\text{FE}}(c)$, obtained using the finite element solution.

c	$k_{\text{PB}}(c)$	$\delta k_{\text{PB}}(c)$	$\delta K_{\text{FE}}(c)$
	Uncorrected $\partial\Omega_R$ ($\sigma_{\max} = 0.1$, $\Gamma = 1$)		
1	1.37 ± 0.02	0.091 ± 0.013	0.123
2	1.80 ± 0.02	0.075 ± 0.014	0.071
4	2.06 ± 0.02	0.024 ± 0.012	0.031
	Corrected $\partial\Omega_R$ ($\sigma_{\max} = 0.099$, $\Gamma = 1.20$)		
1	1.28 ± 0.01	0.019 ± 0.011	0.026
2	1.67 ± 0.02	-0.002 ± 0.013	0.006
4	1.97 ± 0.02	-0.018 ± 0.011	-0.011

TABLE IV.1: The effect of correcting the reaction boundary $\partial\Omega_R$ in particle-based simulations of Reaction (IV.14). The steady-state rate constant $k_{\text{PB}}(c)$ is computed using Equation (IV.16), where the mean of N_A is obtained from 10^4 simulation replicates for $c = 1$ and $c = 2$, and from 1.5×10^4 replicates for $c = 4$. The relative error, $\delta k_{\text{PB}}(c)$, between the simulated steady-state reaction rate and the desired reaction rate is calculated using Equation (IV.17). We also provide the relative error, $\delta K_{\text{FE}}(c)$—calculated from the finite element solution using Equation (IV.11)—for comparison. Results are given for the reaction boundary in Equation (IV.1) both before and after the correction, defined by $\sigma_{\max} = 0.1$, $\Gamma = 1$ and $\sigma_{\max} = 0.099$, $\Gamma = 1.20$, respectively. Here we consider $\hat{D}_1 = 2$ and $\hat{D}_2 = 5.5$.

The boundary correction significantly reduces the magnitude of $\delta K_{\text{PB}}(c)$ for all concentrations considered, and the sum of the squares of the residuals has been reduced from $(3.2 \pm 0.7) \times 10^{-2}$ to $(2 \pm 2) \times 10^{-3}$.

V. DISCUSSION

The leading-order solution P_0 to the steady-state probability density in Equation (II.24) corresponds to the exact solution in the case that $\partial\Omega_R$ is independent of r_2, that is, if $f(r_2)$ is a constant. This simplifies the problem significantly since the probability of finding the state associated with the closest molecule of C with a given r_1 is independent of the probability of finding the same state with a particular r_2. In other words, in this case, Equation (II.19) is separable. However, this simple boundary is equivalent to imposing Smoluchowski's reaction condition on Reaction (I.5) and therefore only yields bimolecular mass-action kinetics. To obtain more complex kinetics, in general $\partial\Omega_R$ will need to be spatially dependent, and a separable solution cannot be found. The degree to which the exact density can be approximated by P_0 depends on how well $\partial\Omega$ is approximated by the flat boundary assumed when deriving P_0. This dependence can be inferred from Figure IV.4 which shows that the steady-state reaction rate $K_{\text{FE}}(c)$ converges to the approximate rate $K_1(c)$, which is constructed from P_0, as Γ reduces since in the limit that $\Gamma \to 0$ the boundary becomes constant.

The approximate steady-state reaction rate $K_1(c)$ neglects $O(\sigma_{\max}^2)$ contributions to the total flux over $\partial\Omega_R$, which amounts to ignoring the $O(\sigma_{\max}^2)$ corrections to P_0 and the flux of the probability density over $\partial\Omega_R$ in the $\hat{r}_2$ direction. In essence, we ignore the diffusive and advective flux of the density in the $\hat{r}_2$ direction and we also neglect any influence this diffusive and advective motion has on the probability density itself. As a consequence, compared to P_h, P_0 underestimates the probability that the closest molecule is close to the origin, see Figure IV.1, while $K_1(c)$ underestimates the contributions of the flux over $\partial\Omega_R$ in both the $\hat{r}_1$ and $\hat{r}_2$ directions, see Figures IV.3 and IV.4. Both corrections to $K_1(c)$ are $O(\sigma_{\max}^2)$ but we find that the correction to the flux over $\partial\Omega_R$ in the $\hat{r}_1$ direction is typically larger in magnitude. Although, as shown in Figure IV.3, this is parameter dependent, and it is possible for the correction in the $\hat{r}_2$ direction to be larger.

Kearney and Flegg [50] also examined the relative error between $K(c)$ and $K_1(c)$ for the particular choice of $\partial\Omega_R$ given in Equation (IV.1). However, they approximated $K(c)$ using the reaction rate obtained from a particle-based simulation of Reaction (I.5), rather than $K_{\mathrm{FE}}(c)$. As a result, for comparable parameter choices, our values for $\delta K(c)$ do not agree with those reported by Kearney and Flegg. In particular, for $c = 10$, $\sigma_{\max} = 0.1$, $\Gamma = 1$, $\hat{D}_1 = 2$ and $\hat{D}_2 = 1.5$, while Kearney and Flegg report a (signed) relative error of less than -2.5×10^{-2} indicating that the simulated rate is less than $K_1(c)$. In comparison, for this choice of parameters, we find that $K_{\mathrm{FE}}(c)$ exceeds $K_1(c)$ and that $\delta K(c) = 7.6 \times 10^{-3}$. In fact, for all parameter combinations considered, we find that the relative error is strictly positive, suggesting that $K_1(c)$ underestimates the true reaction rate.

This disparity arises because the particle-based simulation developed by Kearney and Flegg underestimates the true reaction rate. This occurs because it does not exactly produce the underlying particle dynamics, allowing some reactions to go undetected. The resulting discrepancy is evident in Table IV.1, where $\delta k_{\mathrm{PB}}(c)$ underestimates the expected relative error given by $\delta K_{\mathrm{FE}}(c)$ for the uncorrected boundary when $c = 1$. Although increasing the height of the reaction boundary has been shown to mitigate this issue, we have not applied this adjustment because it would obscure the high-order corrections studied here. Fortunately, such limitations can be overcome using more accurate simulation techniques [43, 44], leaving only the error that arises from using $K_1(c)$ to approximate the reaction rate.

In Subsection IV B we demonstrate how to minimise this source of error by altering the reaction boundary $\partial\Omega_R$. To obtain an analytic expression for $\partial\Omega_R$, we use Equation (II.27) and the inverse Laplace transform to derive a boundary that (approximately) matches the desired reaction rate $K_{\mathrm{D}}(c)$. This assumes that $K_1(c)$ approximates the exact reaction rate, for which $K_{\mathrm{FE}}(c)$ is a proxy, well enough that the corresponding boundary is close enough to the true boundary that reproduces $K_{\mathrm{D}}(c)$ to serve as a good starting point for the optimisation. To retain an analytic expression for $\partial\Omega_R$ we choose to only alter the parameters, $\sigma_{\max}$ and Γ in our case, that define the boundary during the optimisation rather than the functional form of the boundary itself. In essence, we are assuming that the true boundary that corresponds to $K_{\mathrm{D}}(c)$ has the same functional form as the initial boundary determined using Equation (II.27). This is equivalent to assuming that $K_{\mathrm{FE}}(c)$ for a given $\partial\Omega_R$ has the same dependence on the concentration c as the approximation $K_1(c)$, and only the dependence on the boundary parameters differs between the two rates.

Our approach is simple to implement because it relies on the open-source library SciPy, and the optimised boundary is no more difficult to evaluate than the initial boundary. This is particularly important for the efficiency of particle-based simulations, since the value of reaction boundary must be evaluated for each potential reaction event. The corrections can be precomputed for any given chemical system and could be tabulated for common reaction rates to reduce unnecessary computation. Moreover, our results in Table IV.1, demonstrate that such corrections can be applied in practice to improve the accuracy of particle-based simulations.

However, notice that if the concentration is large, then altering $\partial\Omega_R$ can increase rather than decrease the relative error between $K_{\mathrm{FE}}(c)$ and $K_{\mathrm{D}}(c)$. As shown in Figure IV.5, for the initial boundary, determined by Equation (II.27), $K_{\mathrm{FE}}(c)$ will converge to $K_{\mathrm{D}}(c)$ as c increases. This is because as c increases the probability density becomes more localised in r_2 and the likelihood of finding the closest molecule near the origin (at small r_2) increases. Therefore, the portion of $\partial\Omega_R$ over which the flux of the probability density is non-zero continually decreases and becomes localised to small values of r_2. Eventually, the relevant portion of $\partial\Omega_R$ given in Equation (IV.1) can be considered essentially constant and, under such conditions, $K_{\mathrm{FE}}(c)$ is equal to $K_1(c)$. That is, for sufficiently large concentrations, Equation (II.27) yields the correct reaction boundary for the kinetics considered here. Since our approach seeks to minimise the sum of the squares of the residuals across a range of concentrations, the optimisation that will typically improve the error where it is initially large and will potentially make the error worse where it is initially small.

It may be possible to achieve better convergence to the desired reaction rate by allowing the functional form of $\partial\Omega_R$ to be varied during the optimisation. An obvious starting point in this direction would be to model the concentration dependence of the error between $K_{\mathrm{FE}}(c)$ and $K_{\mathrm{D}}(c)$ and then attempt to introduce additional terms to the reaction boundary that account for the differing concentration dependence of $K_{\mathrm{FE}}(c)$ and $K_1(c)$. Furthermore, if we abandon our attachment to a simple analytic expression for $\partial\Omega_R$, one could selectively alter portions of the boundary using machine learning techniques to improve the error for selected values of c, while minimising the adverse effects for concentrations outside this range. Finally, if the range of c can be estimated in advance, then better results can be obtained by performing the optimisation over this application-specific range. However, there exist many biochemical systems in which the concentration of reactants undergo large-scale oscillations [75–77] for which this will not be possible.

VI. CONCLUSION

We considered the evolution of a system that consists of diffusing molecules from three different chemical species labelled A, B, and C. The molecules react whenever the distance r_1 between two molecules of A and B is less than or equal to a function $f(r_2)$ of the distance r_2 to the closest molecule of C. This proximity-based reaction condition

defines a reactive region in the state space of the system on whose surface $(\partial\Omega_R)$ triplets of molecules, where each triplet contains one molecule of A, B and C, are absorbed. We derive a nonlinear partial integro-differential equation, Equation (II.19), which describes the evolution of the probability density to find the closest molecule, relative to a particular pair of A and B molecules, of C at a given position. The proximity-based reaction condition is imposed as an absorbing boundary condition on the governing equation, see Equation (II.21), and the total flux of the probability density over this boundary corresponds to the reaction rate for the system.

By assuming that $\partial\Omega_R$ extends a small distance $\sigma_{\max}$ in the $\hat{\boldsymbol{r}}_1$ direction, we use singular perturbation theory to derive a leading-order solution $(P_0(r_1, r_2))$ for the steady-state probability density. This solution is then used to construct an approximation, $K_1(c)$ defined in Equation (II.27), to the steady-state reaction rate for the system. Both P_0 and $K_1(c)$ neglect corrections of $O(\sigma_{\max}^2)$, which are difficult to study analytically, so we construct finite element solutions P_h and s_h for the probability density and the flux of this density respectively, for the specific choice of $\partial\Omega_R$ defined in Equation (IV.1). Using these solutions, we show that P_0 underestimates the probability of finding the closest molecule of C near the origin, or at small r_2 values as shown in Figure IV.1, while $K_1(c)$ underestimates the reaction rate $K_{\mathrm{FE}}(c)$ obtained from s_h, see Figures IV.3, IV.4 and IV.5.

This is the first time such errors have been quantified, and our results elucidate the source of the errors reported in particle-based simulations of an equivalent system [50]. In Subsection IV B we demonstrate how to correct for these errors in a manner that can be easily and efficiently incorporated into existing simulations. Moreover, our work provides insight into the dynamics of particles within particle-based simulations and should assist in the continual development of novel proximity-based reaction conditions. Although we have only considered a single functional form for $\partial\Omega_R$, our analysis could be extended to other reactive boundaries. So long as the boundary remains monotonically decreasing in r_2 as assumed here, our analysis should extend in a straightforward manner. Violating this assumption complicates matters as the state associated with the closest molecule of C will not necessarily cross the boundary first. If we mandate that reactions only occur when this specific state crosses the boundary, then the dynamics of the system will still be governed by Equation (II.19), but we would expect the behaviour of the examined errors to change since the normal vector to the boundary will sometimes have a component in the opposite direction of $\hat{\boldsymbol{r}}_2$. In these regions, the advective motion described by the final term in Equation (II.19) will push the relevant state away from the reaction boundary, thus decreasing the reaction rate as opposed to always increasing the rate as is the case for a monotonically decreasing boundary.

Appendix A: The evolution of $\Phi(\boldsymbol{\eta_2}, t)$

To derive the governing equation for $\Phi(\boldsymbol{\eta_2}, t)$, we consider $\mathcal{L}_2\Phi(\boldsymbol{\eta_2}, t)$ where

$$\mathcal{L}_2 \equiv \frac{\partial}{\partial t} - \hat{D}_2\hat{\nabla}_2^2, \tag{A.1}$$

is the diffusion operator on the 3-dimensional space spanned by $\boldsymbol{\eta_2}$, originally defined in Equation (II.7a). The time derivative of $\Phi(\boldsymbol{\eta_2}, t)$ is given by

$$\Phi_t = g\phi_t - c\phi g \int_{V_2} \phi_t\left(\boldsymbol{\eta_3'}, t\right) dV_2', \tag{A.2}$$

where we have used the t subscript to denote differentiation with respect to time and defined

$$g \equiv g\left(\boldsymbol{\eta_2}, t\right) = \exp\left(-c\int_{V_2} \varphi\left(\boldsymbol{\eta_2'}, t\right) dV_2'\right), \tag{A.3}$$

for notational convenience. We can also take the Laplacian of Φ with respect to the coordinates of $\boldsymbol{\eta_2}$

$$\hat{\nabla}_2^2\Phi = g\hat{\nabla}_2^2\phi + 2\left(\hat{\nabla}_2\phi\right)\cdot\left(\hat{\nabla}_2 g\right) + \phi\hat{\nabla}_2^2 g, \tag{A.4}$$

which when combined with Equation (A.2) yields

$$\mathcal{L}_2\Phi = g\phi_t - c\phi g \int_{V_2} \phi_t\left(\boldsymbol{\eta_3'}, t\right) dV_2' - \hat{D}_2\left[g\hat{\nabla}_2^2\phi - 2\left(\hat{\nabla}_2\phi\right)\cdot\left(\hat{\nabla}_2 g\right) - \phi\hat{\nabla}_2^2 g\right]. \tag{A.5}$$

Recalling that $\mathcal{L}_2\phi = 0$ from Equation (II.7a) and applying the Divergence theorem we find

$$\begin{aligned}
\mathcal{L}_2\Phi &= \hat{D}_2\left[-c\phi g \int_{V_2} \hat{\nabla}_2^2\phi\left(\boldsymbol{\eta_3'}, t\right) dV_2' - 2\left(\hat{\nabla}_2\phi\right)\cdot\left(\hat{\nabla}_2 g\right) - \phi\hat{\nabla}_2^2 g\right] \\
&= -c\hat{D}_2\phi g \oint_{S_2} \left(\hat{\nabla}_2\phi\left(\boldsymbol{\eta_3'}, t\right)\right)\cdot\hat{\boldsymbol{r}}_2 dA_2' - 2\hat{D}_2\left(\hat{\nabla}_2\phi\right)\cdot\left(\hat{\nabla}_2 g\right) - \hat{D}_2\phi\hat{\nabla}_2^2 g,
\end{aligned} \tag{A.6}$$

where S_2 is the surface of a sphere of radius $r_2 = ||\boldsymbol{\eta}_2||$, dA_2' is an elemental area on that surface and $\hat{\boldsymbol{r}}_2$ is the unit outward facing normal vector. The diffusion in the $\boldsymbol{\eta}_2$ coordinate is isotropic, and so ϕ is independent of orientation. That is, ϕ only has radial dependence, so we have

$$\hat{\nabla}_2 g = \hat{\nabla}_2 \exp\left(-c \int_{V_2} \varphi\left(\boldsymbol{\eta}_2', t\right) dV_2'\right)$$
$$= -cg\phi \left(\oint_{S_2} dA_2'\right) \hat{\boldsymbol{r}}_2. \tag{A.7}$$

By the same reasoning we are able to take the integrand outside the integral in Equation (A.6) and by substituting in Equation (A.7) we obtain

$$\mathcal{L}_2\Phi = -\hat{D}_2\left[\left(\hat{\nabla}_2\phi\right)\cdot\left(\hat{\nabla}_2 g\right) + \phi\hat{\nabla}_2^2 g\right]$$
$$= -\hat{D}_2\hat{\nabla}_2 \cdot \left(\phi\hat{\nabla}_2 g\right)$$
$$= \hat{D}_2\hat{\nabla}_2 \cdot \left(cg\phi^2 \left(\oint_{S_2} dA_2'\right) \hat{\boldsymbol{r}}_2\right) \tag{A.8}$$
$$= \hat{D}_2\hat{\nabla}_2 \cdot \left(4\pi r_2^2 c\phi\Phi\hat{\boldsymbol{r}}_2\right).$$

That is,

$$\frac{\partial\Phi\left(\boldsymbol{\eta}_2, t\right)}{\partial t} = \hat{D}_2\hat{\nabla}_2^2\Phi\left(\boldsymbol{\eta}_2, t\right) + \hat{D}_2\hat{\nabla}_2 \cdot \left(4\pi r_2^2 c\phi\Phi\left(\boldsymbol{\eta}_2, t\right)\hat{\boldsymbol{r}}_2\right), \tag{A.9}$$

as stated in Equation (II.14).

Appendix B: Singular perturbation analysis

To determine the steady-state solution $P\left(r_1, r_2\right)$ of Equation (II.19) near the reaction boundary $\partial\Omega_R$, defined in Equation (II.5), we seek a radial steady-state solution, $\bar{P}\left(u_1, u_2\right) = P\left(r_1, r_2\right)$, where

$$u_1 = \frac{r_1}{\sigma_{\max}} \quad \text{and} \quad u_2 = r_2, \tag{B.1}$$

are scaled radial coordinates. With this change of variables, the steady-state form of Equation (II.19) becomes

$$\frac{\hat{D}_1}{u_1^2} \frac{\partial}{\partial u_1}\left(u_1^2 \frac{\partial\bar{P}\left(u_1, u_2\right)}{\partial u_1}\right) + \frac{\sigma_{\max}^2 \hat{D}_2}{u_2^2} \frac{\partial}{\partial u_2}\left(u_2^2 \frac{\partial\bar{P}\left(u_1, u_2\right)}{\partial u_2} + \frac{u_2^4\left(\bar{P}\left(u_1, u_2\right)\right)^2}{\int_{u_2}^\infty \bar{P}\left(u_1, u_2'\right) u_2'^2 du_2'}\right) = 0, \tag{B.2}$$

while the associated boundary conditions are:

$$\bar{P}\left(u_1, u_2\right) = 0 \quad \text{on} \quad u_1 = F(u_2), \quad \text{where } F(u_2) = \frac{f(u_2)}{\sigma_{\max}}, \tag{B.3a}$$

$$\lim_{u_1\to\infty} \bar{P}\left(u_1, u_2\right) = \frac{c}{V}\exp\left(\frac{-4\pi c u_2^3}{3}\right), \tag{B.3b}$$

$$\lim_{u_2\to\infty} \bar{P}\left(u_1, u_2\right) = \lim_{u_2\to\infty} \frac{c}{V}\exp\left(\frac{-4\pi c u_2^3}{3}\right) = 0 \quad \text{and} \tag{B.3c}$$

$$\frac{\partial\bar{P}\left(u_1, u_2\right)}{\partial u_2} = 0, \quad \text{when } u_2 = 0. \tag{B.3d}$$

Following the change of variables the singular nature of the PDE becomes plain. Very close to $\partial\Omega_R$ diffusion in the $\hat{\boldsymbol{r}}_1$ direction dominates and there is comparatively little diffusive or advective motion in the $\hat{\boldsymbol{r}}_2$ direction, where $\hat{\boldsymbol{r}}_i$ is the unit radial basis vector for $\boldsymbol{\eta}_i$. In the limit that $\sigma_{\max} \to 0$, motion in the $\hat{\boldsymbol{r}}_2$ direction can be ignored, and it is only necessary to consider diffusive flux in the $\hat{\boldsymbol{r}}_1$ direction.

More formally, we assume the solution to Equation (B.2) can be expanded in a perturbation series of the form

$$\bar{P}\left(u_1, u_2\right) = \bar{P}_0\left(u_1, u_2\right) + \sigma_{\max}^2 \bar{P}_1\left(u_1, u_2\right) + O(\sigma_{\max}^4). \tag{B.4}$$

To derive the leading-order solution we substitute this perturbation series into Equation (B.2) and match the $O(1)$ terms which leads to

$$\bar{P}_0\left(u_1, u_2\right) = h_0(u_2)\left(1 - \frac{F(u_2)}{u_1}\right),$$
(B.5)

where h_0 is an arbitrary function of u_2. To determine h_0 we use the matching condition

$$\lim_{u_1 \to \infty} \bar{P}_0\left(u_1, u_2\right) = \frac{c}{V}\exp\left(\frac{-4\pi c u_2^3}{3}\right),$$
(B.6)

which yields

$$\bar{P}_0\left(u_1, u_2\right) = \frac{c}{V}\exp\left(\frac{-4\pi c u_2^3}{3}\right)\left(1 - \frac{F(u_2)}{u_1}\right),$$
(B.7)

and amounts to requiring that in the bulk, far from $\partial\Omega_R$, the absorption of states on $\partial\Omega_R$ causes a negligible perturbation in the solution. Finally, reverting to our original coordinates r_1 and r_2 we recover the approximate steady-state solution

$$P_0\left(r_1, r_2\right) = \frac{c}{V}\exp\left(\frac{-4\pi c r_2^3}{3}\right)\left(1 - \frac{f(r_2)}{r_1}\right),$$

stated in Equation (II.24) of the main text.

The results presented in the main text indicate that P_0 is indeed the dominant term in the perturbation expansion of P. However, as shown below, the standard expansion in Equation (B.4) cannot be used to obtain higher-order corrections to the solution. Instead, these corrections have been quantified using finite element methods, as detailed in the main text.

In an attempt to determine the $O(\sigma_{\max}^2)$ correction to the solution we once again substitute the perturbation series into Equation (B.2) only now we match terms to $O(\sigma_{\max}^2)$ to obtain

$$\frac{\hat{D}_1}{u_1^2}\frac{\partial}{\partial u_1}\left(u_1^2\frac{\partial\bar{P}_1(u_1, u_2)}{\partial u_1}\right) + \frac{\hat{D}_2}{u_2^2}\frac{\partial}{\partial u_2}\left(u_2^2\frac{\partial\bar{P}_0(u_1, u_2)}{\partial u_2} + \frac{u_2^4\left(\bar{P}_0(u_1, u_2)\right)^2}{\int_{u_2}^{\infty}\bar{P}_0(u_1, u_2')u_2'^2 du_2'}\right) = 0.$$
(B.8)

To arrive at Equation (B.8) we have used the fact that

$$\frac{\hat{D}_1}{u_1^2}\frac{\partial}{\partial u_1}\left(u_1^2\frac{\partial\bar{P}_0(u_1, u_2)}{\partial u_1}\right) = 0,$$
(B.9)

and performed a Taylor series expansion about $\sigma_{\max}^2 = 0$ to write

$$\frac{1}{\int_{u_2}^{\infty}(\bar{P}(u_1, u_2'))u_2'^2 du_2'} = \frac{1}{I_0(u_2)}\frac{1}{1 + \frac{\sigma_{\max}^2}{I_0(u_2)}(I_1(u_2) + O(\sigma_{\max}^2))}$$
(B.10)

$$= \frac{1}{I_0(u_2)}\left(1 - \sigma_{\max}^2\frac{I_1(u_2)}{I_0(u_2)} + O(\sigma_{\max}^4)\right),$$
(B.11)

where $I_i(u_2) = \int_{u_2}^{\infty}(\bar{P}_i(u_1, u_2'))u_2'^2 du_2'$. To satisfy the condition in Equation (B.3a) we require

$$\bar{P}_1(u_1, u_2) = 0 \quad \text{on} \quad u_1 = F(u_2),$$
(B.12)

and the corresponding solution is

$$\bar{P}_1(u_1, u_2) = \left(\int_{F(u_2)}^{u_1}\left(1 - \frac{\xi}{u_1}\right)\xi\mathcal{L}_{u_2}\bar{P}_0(\xi, u_2)d\xi + h_1(u_2)\left(1 - \frac{F(u_2)}{u_1}\right)\right),$$
(B.13)

where

$$\mathcal{L}_{u_2}\bar{P}_0(u_1, u_2) \equiv -\frac{\hat{D}_2}{\hat{D}_1 u_2^2}\frac{\partial}{\partial u_2}\left(u_2^2\frac{\partial\bar{P}_0(u_1, u_2)}{\partial u_2} + \frac{u_2^4\left(\bar{P}_0(u_1, u_2)\right)^2}{\int_{u_2}^{\infty}\bar{P}_0(u_1, u_2')u_2'^2 du_2'}\right),$$
(B.14)

ultimately depends on the reaction boundary $\partial\Omega_R$ and can be computed using Equation (B.7).

The arbitrary function $h_1(u_2)$ is determined by the matching condition

$$\lim_{u_1 \to \infty} \bar{P}_1(u_1, u_2) = 0, \tag{B.15}$$

which is required to satisfy Equation (B.3b). This condition can only be satisfied, by choosing h_1 appropriately, if the integral in Equation (B.13) remains bounded as $u_1 \to \infty$. In general, however, this integral diverges in the limit $u_1 \to \infty$ because the term $\xi\mathcal{L}_{u_2}\bar{P}_0(\xi, u_2)$ tends to infinity as $\xi \to \infty$. An exception arises when the leading-order solution $\bar{P}_0$ is also a solution to the homogeneous equation associated with the differential operator $\mathcal{L}_{u_2}$, as occurs, for example, when $\partial\Omega_R$—and hence $F(r_2)$—is constant. In that case, $\bar{P}_1$ vanishes identically since $\bar{P}_0$ is the exact solution to the original PDE in Equation (B.2). The failure to satisfy the matching condition in the general case indicates that the assumed form of the perturbation series in Equation (B.4) is not appropriate beyond $O(1)$.

Appendix C: Finite element discretisation

All routines described in this appendix have been implemented using the open-source finite element library `FEniCS` [78], and a publicly available repository [79] contains the main codes required to reproduce the simulations presented in Section IV.

Before stating the finite element formulation of Equation (III.4), let us recall, for a sufficiently smooth vector-valued function $\boldsymbol{\tau} = (\tau_1, \tau_2)^T$ and a scalar function v, the following integration by parts formula for radial coordinates. This employs the two-dimensional gradient from Equation (III.2), usual two-dimensional divergence $\nabla_c \cdot \boldsymbol{\tau} = \partial_{r_1}\tau_1 + \partial_{r_2}\tau_2$, radial divergence from Equation (III.6) (noting that $\nabla \cdot \boldsymbol{\tau} = \nabla_c \cdot \boldsymbol{\tau} + \frac{2}{r_1}\tau_1 + \frac{2}{r_2}\tau_2$), and usual integration by parts in two-dimensions:

$$
\begin{aligned}
\int_{\Omega_{\text{FE}}} (\nabla \cdot \boldsymbol{\tau})(v\omega)\, dr_2\, dr_1 &= \int_{\Omega_{\text{FE}}} (\nabla_c \cdot \boldsymbol{\tau})(v\omega)\, dr_2\, dr_1 + \int_{\Omega_{\text{FE}}} 2\left(\frac{\omega}{r_1}\tau_1 + \frac{\omega}{r_2}\tau_2\right) v\, dr_2\, dr_1 \\
&= \int_{\partial\Omega_{\text{FE}}} (\boldsymbol{\tau} \cdot \boldsymbol{n})(v\omega)\, ds - \int_{\Omega_{\text{FE}}} (\boldsymbol{\tau} \cdot \nabla v)\,\omega\, dr_2\, dr_1 \\
&\quad - \int_{\Omega_{\text{FE}}} (\boldsymbol{\tau} \cdot \nabla\omega) v\, dr_2\, dr_1 + \int_{\Omega_{\text{FE}}} 2\left(\frac{\omega}{r_1}\tau_1 + \frac{\omega}{r_2}\tau_2\right) v\, dr_2\, dr_1 \\
&= \int_{\partial\Omega_{\text{FE}}} (\boldsymbol{\tau} \cdot \boldsymbol{n})(v\omega)\, ds - \int_{\Omega_{\text{FE}}} (\boldsymbol{\tau} \cdot \nabla v)\,\omega\, dr_2\, dr_1.
\end{aligned} \tag{C.1}
$$

Here $\omega = (4\pi r_1 r_2)^2$ denotes the weight associated with the radial coordinates r_1 and r_2, while $\partial\Omega_{\text{FE}}$ denotes the boundary of Ω_{FE} which we divide into four segments: Γ_{left}, Γ_{bot}, Γ_{right} and Γ_{top}, defined by the regions $r_2 = 0$, $r_1 = f(r_2)$, $r_2 = r_2^{\max}$ and $r_1 = r_1^{\max}$ respectively. A sketch of an unstructured triangular mesh having more refinement near the absorbing boundary $\Gamma_{\text{bot}} = \partial\Omega_R$, and identifying all sub-boundaries is shown in Figure C.1.

Consider now a finite element mesh $\mathcal{T}_h$—an unstructured partition of the domain Ω_{FE} into triangles K—of maximum diameter $h = \{\max h_K : K \in \mathcal{T}_h\}$. Let us denote by $\mathcal{E}_h$ the set of all interior edges e with length h_e (and $\mathcal{E}_h^\partial$ denotes the boundary edges). In addition, we use $[\![s]\!]_e$ to denote the jump of a scalar field s across the edge e. Proceeding from a weak formulation of (III.4) (derived from the integration by parts in radial coordinates (C.1) and using the mixed type boundary conditions – for the flux essentially, and for the density and density moment naturally) and considering a mixed-primal Galerkin discretisation, the finite element formulation consists in finding the approximate unknowns of flux $\boldsymbol{s}_h$, density P_h, and density moment Q_h in the discrete spaces $\Sigma_h \times \Phi_h \times \Psi_h$, such that

$$
\begin{aligned}
\int_{\Omega_{\text{FE}}} \boldsymbol{s}_h \cdot D\boldsymbol{\tau}_h \omega\, dr_2\, dr_1 &- \int_{\Omega_{\text{FE}}} P_h \nabla \cdot (D\boldsymbol{\tau}_h)\omega\, dr_2\, dr_1 + \int_{\Omega_{\text{FE}}} \left(\frac{r_2^2 P_h^2}{Q_h}\hat{\boldsymbol{r}}_2\right) \cdot (D\boldsymbol{\tau}_h)\omega\, dr_2\, dr_1 = \\
&- \int_{\Gamma_{\text{right}}} P_{\text{right}} D\boldsymbol{\tau}_h \cdot \boldsymbol{n}\omega ds - \int_{\Gamma_{\text{bot}}} P_{\text{bot}} D\boldsymbol{\tau}_h \cdot \boldsymbol{n}\omega ds - \int_{\Gamma_{\text{top}}} P_{\text{top}} D\boldsymbol{\tau}_h \cdot \boldsymbol{n}\omega ds \qquad \forall \boldsymbol{\tau}_h \in \Sigma_h^0,
\end{aligned} \tag{C.2a}
$$

$$
-\int_{\Omega_{\text{FE}}} v_h \nabla \cdot (D\boldsymbol{s}_h)\omega\, dr_2\, dr_1 = 0 \qquad \forall v_h \in \Phi_h, \tag{C.2b}
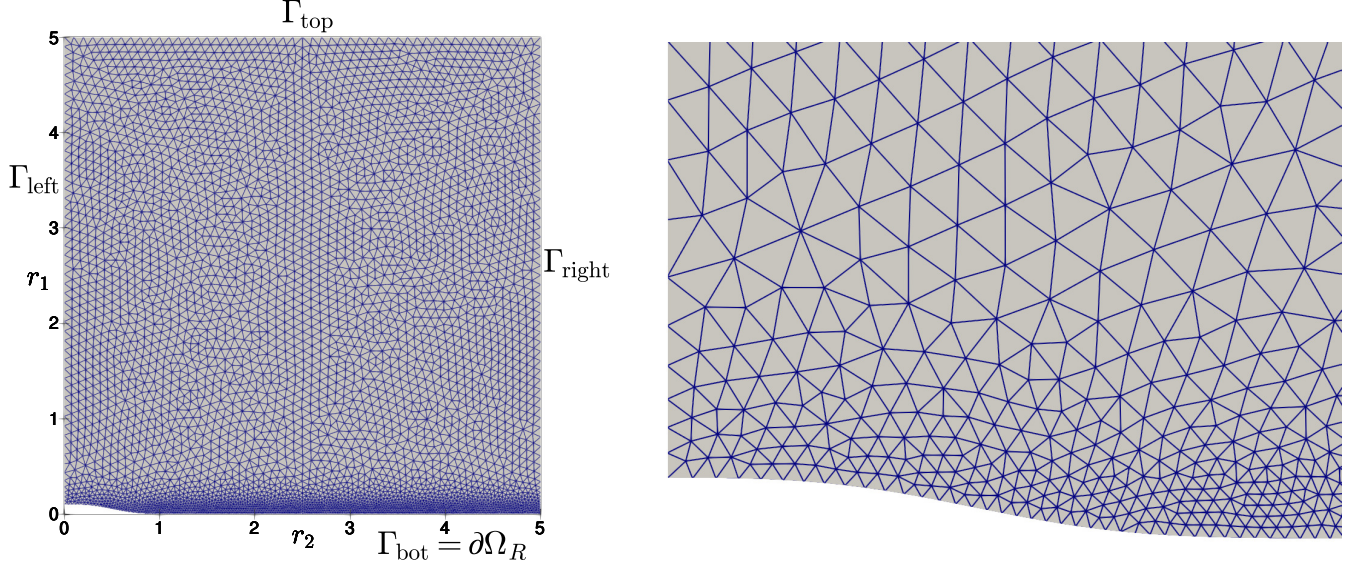$$

FIG. C.1: Unstructured triangular mesh and boundary configuration of the computational domain (left), and zoom into the bottom left corner showing the mesh refinement near the absorbing boundary (right panel).

$$\int_{\Omega_{\mathrm{FE}}} (r_2^2 P_h - \nabla \cdot \hat{\boldsymbol{r}}_2 Q_h) w_h \omega \, \mathrm{d}r_2 \, \mathrm{d}r_1 - \int_{\Omega_{\mathrm{FE}}} (\nabla w_h \cdot \hat{\boldsymbol{r}}_2) Q_h \omega \, \mathrm{d}r_2 \, \mathrm{d}r_1 + \int_{\Gamma_{\mathrm{left}}} \hat{\boldsymbol{r}}_2 \cdot \boldsymbol{n} Q_h w_h \omega \mathrm{d}s$$

$$+ \sigma_{\mathrm{stab}} \sum_{e \in \mathcal{E}_h} \frac{h_e^2}{(k+1)^\alpha} \beta \int_e [\![\nabla Q_h \cdot \boldsymbol{n}_e]\!]_e [\![\nabla w_h \cdot \boldsymbol{n}_e]\!]_e \omega \mathrm{d}s$$

$$+ \sigma'_{\mathrm{stab}} \sum_{h_e \in \mathcal{E}_h^\partial} \left(h_e [\hat{\boldsymbol{r}}_2 \cdot \boldsymbol{n}]_-^2 + \frac{8}{h_e} \right) \int_e Q_h w_h \omega \mathrm{d}s =$$

$$\int_{\Gamma_{\mathrm{right}}} \hat{\boldsymbol{r}}_2 \cdot \boldsymbol{n} Q_{\mathrm{right}} w_h \omega \mathrm{d}s + \sigma'_{\mathrm{stab}} \sum_{h_e \in \mathcal{E}_h^\partial} \left(h_e [\hat{\boldsymbol{r}}_2 \cdot \boldsymbol{n}]_-^2 + \frac{8}{h_e} \right) \int_e Q_\partial w_h \omega \mathrm{d}s \qquad \forall w_h \in \Psi_h. \tag{C.2c}$$

The discrete trial and test spaces for the flux-density pair are, for given $k \geq 0$, Raviart–Thomas elements of degree k and overall discontinuous and piecewise polynomials of degree k, while for the density moment we take overall continuous and piecewise polynomials of degree $k+1$ (see their precise definition for the Cartesian case in, e.g., [80] and the modification for axisymmetric divergence in [81], see also [82, 83]):

$$\Sigma_h := \{\boldsymbol{\tau}_h \in \mathbf{H}(\mathrm{div}_r; \Omega_{\mathrm{FE}}) : \boldsymbol{\tau}_h|_K \in \mathbb{RT}_k(K) \; \forall K \in \mathcal{T}_h, \; \boldsymbol{\tau}_h \cdot \boldsymbol{n}|_{\Gamma_{\mathrm{left}}} = s_{\mathrm{left}}\}, \tag{C.3a}$$

$$\Sigma_h^0 := \{\boldsymbol{\tau}_h \in \mathbf{H}(\mathrm{div}_r; \Omega_{\mathrm{FE}}) : \boldsymbol{\tau}_h|_K \in \mathbb{RT}_k(K) \; \forall K \in \mathcal{T}_h, \; \boldsymbol{\tau}_h \cdot \boldsymbol{n}|_{\Gamma_{\mathrm{left}}} = 0\}, \tag{C.3b}$$

$$\Phi_h := \{v_h \in L_\omega^2(\Omega_{\mathrm{FE}}) : v_h|_K \in \mathbb{P}_k(K) \; \forall K \in \mathcal{T}_h\}, \tag{C.3c}$$

$$\Psi_h := \{w_h \in C^0(\overline{\Omega_{\mathrm{FE}}}) : w_h|_K \in \mathbb{P}_{k+1}(K) \; \forall K \in \mathcal{T}_h\}. \tag{C.3d}$$

Here by $\mathbf{H}(\mathrm{div}_r; \Omega_{\mathrm{FE}})$ we mean all vector fields in $\mathbf{L}_\omega^2(\Omega_{\mathrm{FE}})$ such that their *radial* divergence (III.6) is in the scalar version of the space, $L_\omega^2(\Omega_{\mathrm{FE}})$. In turn, for all $p > 1$, by $L_\omega^p(\Omega_{\mathrm{FE}})$ we denote the weighted Lebesgue space of all measurable functions v on Ω_{FE} such that (see [84])

$$\|v\|_{L_\omega^p(\Omega_{\mathrm{FE}})}^p := \int_{\Omega_{\mathrm{FE}}} |v|^p \omega \, \mathrm{d}r_2 \, \mathrm{d}r_1 < \infty.$$

Observe that in the discrete weak formulation we have tested the constitutive equation for the flux against a weighted test function $D\boldsymbol{\tau}_h$ in order to obtain a block-symmetric structure in the weighted divergence operator. Note also, that since the equation for Q_h is hyperbolic in nature, we employ a continuous interior penalty (C0IP) approach adopted from [85], that restores the otherwise suboptimal convergence expected when using the space Ψ_h. This method includes an additional integration by parts (that we conduct using the modified form (C.1)) and the interior jump penalisation associated with the normal gradients. Other possible choices are classical streamline upwind Petrov–Galerkin or streamline diffusion variants. More details can be found in, e.g., [85, 86].

DoF	h	$e(\boldsymbol{s})$	$r(\boldsymbol{s})$	$e(P)$	$r(P)$	$e(Q)$	$r(Q)$	Memory	CPU
				Lowest-order method with $k = 0$					
33	0.7071	2.93e+01	$\star$	1.03e+00	$\star$	4.92e+00	$\star$	91.55	1.23
113	0.3536	1.73e+01	0.763	5.56e-01	0.888	7.08e+00	-0.526	91.88	1.37
417	0.1768	9.96e+00	0.793	2.84e-01	0.969	1.84e+00	1.943	95.04	1.38
1601	0.0884	5.93e+00	0.747	1.43e-01	0.992	7.10e-01	1.375	10.29	1.41
6273	0.0442	3.72e+00	0.673	7.16e-02	0.997	3.35e-01	1.085	127.33	1.64
24833	0.0221	2.45e+00	0.604	3.59e-02	0.995	1.63e-01	1.036	274.12	3.24
98817	0.0110	1.67e+00	0.551	1.82e-02	0.981	8.13e-02	1.004	730.17	9.21
				Scheme with $k = 1$					
97	0.7071	1.25e+01	$\star$	1.92e-01	$\star$	3.60e+00	$\star$	91.92	1.78
353	0.3536	4.35e+00	1.522	7.00e-02	1.456	1.10e+00	1.717	94.76	1.64
1345	0.1768	1.41e+00	1.625	1.86e-02	1.916	1.81e-01	2.602	110.09	1.75
5249	0.0884	4.79e-01	1.557	4.70e-03	1.981	4.79e-02	1.914	149.36	1.87
20737	0.0442	1.74e-01	1.457	1.18e-03	1.995	1.26e-02	1.929	299.89	3.10
82433	0.0221	6.84e-02	1.350	2.95e-04	1.999	3.21e-03	1.972	984.45	8.05
328705	0.0110	2.89e-02	1.245	7.38e-05	2.000	8.07e-04	1.990	3673.87	34.44

TABLE C.1: Error history (error decay with respect to the number of degrees of freedom of the product discrete space, and experimental convergence rates) with respect to manufactured smooth solutions using the mixed-primal C0IP method with two different polynomial degrees. We also show peak memory usage per mesh refinement (in MB), as well as CPU time (in s).

We confirm experimentally the convergence of (C.2) to the unique weak solution of (III.4) by using smooth manufactured solutions $P(r_1, r_2) = \sin(\pi r_2) \sin(\pi r_1)$, $Q(r_1, r_2) = \frac{3}{2} + \cos(\pi r_1 r_2)$, and considering a manufactured right-hand side for the second and third equations of (III.4). We impose natural boundary conditions for P_h on the right, bottom, and top parts of the boundary, essential boundary conditions for the flux on Γ_{left} and natural boundary conditions for Q_h on the boundary Γ_{right} (the prescribed boundary values and source terms are not necessarily homogeneous but given by the manufactured exact density and density moment). We impose the latter conditions naturally since the upstream mechanism does not permit us to set up a boundary condition essentially on the right boundary (as this can be considered an outflow segment on which $\hat{\boldsymbol{r}}_2 \cdot \boldsymbol{n} > 0$). This explains the additional terms on $\mathcal{E}_h^{\partial}$ suggested in [87]. A sequence of successively refined meshes is constructed, and on each level the approximate solutions are compared to the exact ones using the natural norms

$$e(\boldsymbol{s}) := \|\boldsymbol{s} - \boldsymbol{s}_h\|_{\mathbf{H}(\text{div}_r; \Omega_{\text{FE}})}, \quad e(P) := \|P - P_h\|_{L_\omega^2(\Omega_{\text{FE}})}, \quad e(Q) := \|Q - Q_h\|_{H_\omega(\Omega_{\text{FE}})},$$

and experimental convergence rates are computed as $r_{l+1}(\cdot) = \log(e_{l+1}(\cdot)/e_l(\cdot))[\log(h_{l+1}/h_l)]^{-1}$, where e_l denotes the error incurred at the refinement level with a mesh of size h_l. Here

$$\| \bullet \|_{H_\omega(\Omega_{\text{FE}})}^2 = \| \bullet \|_{L_\omega^2(\Omega_{\text{FE}})}^2 + \int_{\Omega_{\text{FE}}} |\hat{\boldsymbol{r}}_2 \cdot \nabla(\bullet)|^2 \omega \, \mathrm{d}r_2 \, \mathrm{d}r_1$$

is the norm in the graph space. The constants are taken as $\hat{D}_1 = 2$, $\hat{D}_2 = 1.5$, and we test the schemes with polynomial degrees $k = 0$ and $k = 1$. The numerical parameters associated with the C0IP discretisation (C.2c) are taken as $\alpha = \frac{7}{2}$, $\beta = 1$, $\sigma_{\text{stab}} = 0.1$, and $\sigma'_{\text{stab}} = k + 1$.

The results are presented in Table C.1, exhibiting optimal convergence for the density $O(h^{k+1})$, while the flux shows a sub-optimal error decay at $O(h^{k+1/2})$ (a sub-optimal convergence has been shown theoretically in [83] for axisymmetric Darcy equations approximated by lowest-order Raviart–Thomas elements). All unknowns exhibit an optimal convergence (in the sense that this is the approximability property of the chosen finite element spaces). We also report on the required CPU time and peak memory usage per each mesh refinement. Other tests (not shown here) confirm that if we do not use the C0IP strategy, while for the lowest-order case the density moment has optimal convergence, for the case $k = 1$ we obtain only a $O(h)$ convergence. We also plot the components of the approximate solution in Figure C.2. For this test, for every mesh refinement and polynomial degree the Newton–Raphson algorithm used for the nonlinear system has taken no more than four iterations to achieve the desired convergence criterion.
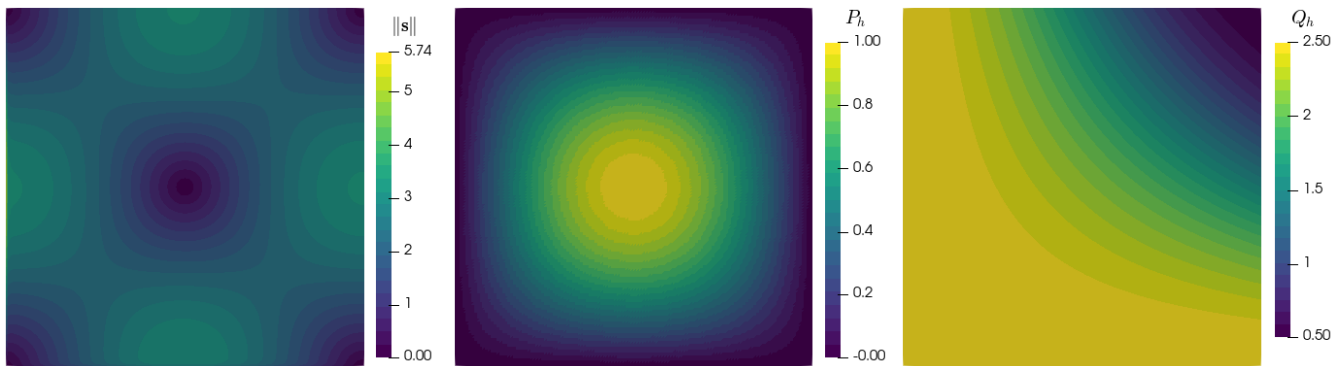
FIG. C.2: Approximate solutions for the convergence test, computed with the lowest-order finite element scheme and shown on a coarse mesh.

[1] M. H. Jacobs, Diffusion processes, in *Diffusion Processes* (Springer Berlin Heidelberg, Berlin, Heidelberg, 1935) Chap. Diffusion Processes, pp. 1–145.

[2] S. S. Mogre, A. I. Brown, and E. F. Koslover, Getting around the cell: physical transport in the intracellular world, Physical Biology **17**, 061003 (2020).

[3] A. L. Koch, Diffusion the crucial process in many aspects of the biology of bacteria, in *Advances in Microbial Ecology* (Springer US, Boston, MA, 1990) Chap. Diffusion The Crucial Process in Many Aspects of the Biology of Bacteria, pp. 37–70.

[4] D. P. Jones, Intracellular diffusion gradients of O_2 and ATP, American Journal of Physiology-Cell Physiology **250**, C663 (1986).

[5] S. T. Kinsey, B. R. Locke, and R. M. Dillaman, Molecules in motion: influences of diffusion on metabolic structure and function in skeletal muscle, Journal of Experimental Biology **214**, 263 (2011).

[6] B. N. Kholodenko and W. Kolch, Giving space to cell signaling, Cell **133**, 566 (2008).

[7] F. Ye, D. K. Breslow, E. F. Koslover, A. J. Spakowitz, W. J. Nelson, and M. V. Nachury, Single molecule imaging reveals a major role for diffusion in the exploration of ciliary space by signaling receptors, Elife **2**, e00654 (2013).

[8] R. J. McMurtrey, Roles of diffusion dynamics in stem cell signaling and three-dimensional tissue development, Stem Cells and Development **26**, 1293 (2017).

[9] A. M. North, Diffusion-controlled reactions, Quarterly Reviews, Chemical Society **20**, 421 (1966).

[10] B. Alberts, A. Johnson, J. Lewis, D. Morgan, and M. Raff, *Molecular Biology of the Cell* (Taylor & Francis Group, Oxford, UK, 2014).

[11] J. D. Murray, *Mathematical biology:v I. An introduction*, Vol. 17 (Springer Science & Business Media, 2007) p. 175.

[12] W. W. Chen, M. Niepel, and P. K. Sorger, Classic and contemporary approaches to modeling biochemical reactions, Genes & Development **24**, 1861 (2010).

[13] S. Soh, M. Byrska, K. Kandere-Grzybowska, and B. A. Grzybowski, Reaction-diffusion systems in intracellular molecular transport and control, Angewandte Chemie International Edition **49**, 4170 (2010).

[14] S. Kondo and T. Miura, Reaction-diffusion model as a framework for understanding biological pattern formation, Science **329**, 1616 (2010).

[15] P. C. Bressloff, *Stochastic processes in cell biology*, Vol. 41 (Springer, 2022).

[16] H. H. McAdams and A. Arkin, It's a noisy business! Genetic regulation at the nanomolar scale, Trends in genetics **15**, 65 (1999).

[17] R. Losick and C. Desplan, Stochasticity and cell fate, Science **320**, 65 (2008).

[18] E. Roberts, A. Magis, J. O. Ortiz, W. Baumeister, and Z. Luthey-Schulten, Noise contributions in an inducible genetic switch: A whole-cell simulation study, PLOS Computational Biology **7**, 1 (2011).

[19] P. J. Halling, Do the laws of chemistry apply to living cells?, Trends in Biochemical Sciences **14**, 317 (1989).

[20] R. Erban and S. J. Chapman, Stochastic modelling of reaction–diffusion processes: algorithms for bimolecular reactions, Physical Biology **6**, 046001 (2009).

[21] S. Smith and R. Grima, Spatial stochastic intracellular kinetics: A review of modelling approaches, Bulletin of Mathematical Biology **81**, 2960 (2019).

[22] D. T. Gillespie, A rigorous derivation of the chemical master equation, Physica A: Statistical Mechanics and its Applications **188**, 404 (1992).

[23] T. Turner, S. Schnell, and K. Burrage, Stochastic approaches for modelling in vivo reactions, Computational Biology and Chemistry **28**, 165 (2004).

[24] T. Jahnke and W. Huisinga, Solving the chemical master equation for monomolecular reaction systems analytically, Journal

of Mathematical Biology **54**, 1 (2007).

[25] D. T. Gillespie, A general method for numerically simulating the stochastic time evolution of coupled chemical reactions, Journal of Computational Physics **22**, 403 (1976).

[26] D. T. Gillespie, Exact stochastic simulation of coupled chemical reactions, The Journal of Physical Chemistry **81**, 2340 (1977).

[27] D. Bernstein, Simulating mesoscopic reaction-diffusion systems using the gillespie algorithm, Phys. Rev. E **71**, 041103 (2005).

[28] S. Lampoudi, D. T. Gillespie, and L. R. Petzold, The multinomial simulation algorithm for discrete stochastic simulation of reaction-diffusion systems, The Journal of Chemical Physics **130**, 094104 (2009).

[29] S. A. Isaacson, The reaction-diffusion master equation as an asymptotic approximation of diffusion to a small target, SIAM Journal on Applied Mathematics **70**, 77 (2009).

[30] M. Malek-Mansour and J. Houard, A new approximation scheme for the study of fluctuations in nonuniform nonequilibrium systems, Physics Letters A **70**, 366 (1979).

[31] J. Elf and M. Ehrenberg, Spontaneous separation of bi-stable biochemical systems into spatial domains of opposite phases, Systems biology **1**, 230 (2004).

[32] J. Hattne, D. Fange, and J. Elf, Stochastic reaction-diffusion simulation with MesoRD, Bioinformatics **21**, 2923 (2005).

[33] S. Engblom, L. Ferm, A. Hellander, and P. Lötstedt, Simulation of stochastic reaction-diffusion processes on unstructured meshes, SIAM Journal on Scientific Computing **31**, 1774 (2009).

[34] I. Hepburn, W. Chen, S. Wils, and E. De Schutter, STEPS: efficient simulation of stochastic reaction–diffusion models in realistic morphologies, BMC systems biology **6**, 1 (2012).

[35] S. A. Isaacson, A convergent reaction-diffusion master equation, The Journal of Chemical Physics **139**, 054101 (2013).

[36] A. Hospital, J. R. Goñi, M. Orozco, and J. L. Gelpí, Molecular dynamics simulations: advances and applications, Advances and Applications in Bioinformatics and Chemistry **8**, 37 (2015).

[37] M. Orozco, L. Orellana, A. Hospital, A. N. Naganathan, A. Emperador, O. Carrillo, and J. Gelpí, Coarse-grained representation of protein flexibility. Foundations, successes, and shortcomings, in *Computational chemistry methods in structural biology*, Advances in Protein Chemistry and Structural Biology, Vol. 85, edited by C. Christov (Academic Press, 2011) pp. 183–215.

[38] M. Feig and Y. Sugita, Whole-cell models and simulations in molecular detail, Annual Review of Cell and Developmental Biology **35**, 191 (2019).

[39] J. Schöneberg, A. Ullrich, and F. Noé, Simulation tools for particle-based reaction-diffusion dynamics in continuous space, BMC Biophysics **7**, 1 (2014).

[40] M. V. Smoluchowski, Versuch einer mathematischen theorie der koagulationskinetik kolloider lösungen, Zeitschrift Für Physikalische Chemie **92**, 129 (1917).

[41] J. S. van Zon and P. R. ten Wolde, Simulating biochemical networks at the particle level and in time and space: Green's function reaction dynamics, Physical Review Letters **94**, 128103 (2005).

[42] J. S. van Zon and P. R. ten Wolde, Green's-function reaction dynamics: A particle-based approach for simulating biochemical networks in time and space, The Journal of Chemical Physics **123**, 234910 (2005).

[43] K. Takahashi, S. Tănase-Nicola, and P. R. ten Wolde, Spatio-temporal correlations can drastically change the response of a MAPK pathway, Proceedings of the National Academy of Sciences **107**, 2473 (2010).

[44] T. R. Sokolowski, J. Paijmans, L. Bossen, T. Miedema, M. Wehrens, N. B. Becker, K. Kaizu, K. Takahashi, M. Dogterom, and P. R. ten Wolde, eGFRD in all dimensions, The Journal of Chemical Physics **150**, 054108 (2019).

[45] S. S. Andrews and D. Bray, Stochastic simulation of chemical reactions with spatial resolution and single molecule detail, Physical Biology **1**, 137 (2004).

[46] J. Schöneberg and F. Noé, Readdy - A software for particle-based reaction-diffusion dynamics in crowded cellular environments, PLOS ONE **8**, 1 (2013).

[47] S. A. Rice, Chapter 2 diffusion-controlled reactions in solution, in *Diffusion-Limited Reactions*, Comprehensive Chemical Kinetics, Vol. 25, edited by C. Bamford, C. Tipper, and R. Compton (Elsevier, 1985) pp. 3–46.

[48] F. C. Collins and G. E. Kimball, Diffusion-controlled reaction rates, Journal of Colloid Science **4**, 425 (1949).

[49] M. Doi, Stochastic theory of diffusion-controlled reaction, Journal of Physics A: Mathematical and General **9**, 1479 (1976).

[50] T. Kearney and M. B. Flegg, Enzyme kinetics simulation at the scale of individual particles, The Journal of Chemical Physics **161**, 194111 (2024).

[51] M. B. Flegg, Smoluchowski reaction kinetics for reactions of any order, SIAM Journal on Applied Mathematics **76**, 1403 (2016).

[52] S. Redner and D. ben Avraham, Nearest-neighbour distances of diffusing particles from a single trap, Journal of Physics A: Mathematical and General **23**, L1169 (1990).

[53] S. Chandrasekhar, Stochastic problems in physics and astronomy, Rev. Mod. Phys. **15**, 1 (1943).

[54] Z. Koza, T. Yanir, and H. Taitelbaum, Nearest-neighbor distance at a single mobile trap, Phys. Rev. E **58**, 6821 (1998).

[55] A. D. Sánchez, M. A. Rodriguez, and H. S. Wio, Results in trapping reactions for mobile particles and a single trap, Phys. Rev. E **57**, 6390 (1998).

[56] K. Kang and S. Redner, Scaling approach for the kinetics of recombination processes, Phys. Rev. Lett. **52**, 955 (1984).

[57] F. Leyvraz and S. Redner, Spatial structure in diffusion-limited two-species annihilation, Phys. Rev. A **46**, 3132 (1992).

[58] A. Donev, J. Rockwell, and D. Ben-Avraham, Generalized von Smoluchowski model of reaction rates, with reacting particles and a mobile trap, Journal of statistical physics **95**, 97 (1999).

[59] M. K. Kadalbajoo and K. C. Patidar, Singularly perturbed problems in partial differential equations: a survey, Applied

Mathematics and Computation **134**, 371 (2003).

[60] J. C. Neu, *Singular perturbation in the physical sciences*, Vol. 167 (American Mathematical Soc., 2015).

[61] H.-G. Roos, H.-G. Roos, M. M. Stynes, and L. L. Tobiska, *Robust numerical methods for singularly perturbed differential equations: convection-diffusion-reaction and flow problems*, 2nd ed., Springer series in computational mathematics, 24 (Springer, Berlin, 2008) pp. 235–421.

[62] R. Lin and M. Stynes, A balanced finite element method for singularly perturbed reaction-diffusion problems, SIAM Journal on Numerical Analysis **50**, 2729 (2012).

[63] K. Khari and V. Kumar, An efficient numerical technique for solving nonlinear singularly perturbed reaction diffusion problem, Journal of mathematical chemistry **60**, 1356 (2022).

[64] D. L. Ermak and J. A. McCammon, Brownian dynamics with hydrodynamic interactions, The Journal of Chemical Physics **69**, 1352 (1978).

[65] A. L. Edelstein and N. Agmon, Brownian dynamics simulations of reversible reactions in one dimension, The Journal of Chemical Physics **99**, 5396 (1993).

[66] J. Lipková, K. C. Zygalakis, S. J. Chapman, and R. Erban, Analysis of Brownian dynamics simulations of reversible bimolecular reactions, SIAM Journal on Applied Mathematics **71**, 714 (2011).

[67] H. Schlichting (Deceased) and K. Gersten, Fundamentals of boundary–layer theory, in *Boundary–Layer Theory* (Springer Berlin Heidelberg, Berlin, Heidelberg, 2017) Chap. Fundamentals of Boundary–Layer Theory, pp. 29–49.

[68] R. Becker, D. Capatina, and R. Luce, Local flux reconstructions for standard finite element methods on triangular meshes, SIAM Journal on Numerical Analysis **54**, 2684 (2016).

[69] G. N. Gatica, A simple introduction to the mixed finite element method, Theory and Applications. Springer Briefs in Mathematics. Springer, London (2014).

[70] D. Angeli, J. E. Ferrell, and E. D. Sontag, Detection of multistability, bifurcations, and hysteresis in a large class of biological positive-feedback systems, Proceedings of the National Academy of Sciences **101**, 1822 (2004).

[71] T. Wilhelm, The smallest chemical reaction system with bistability, BMC Systems Biology **3**, 1 (2009).

[72] M. A. Branch, T. F. Coleman, and Y. Li, A subspace, interior, and conjugate gradient method for large-scale bound-constrained minimization problems, SIAM Journal on Scientific Computing **21**, 1 (1999), https://doi.org/10.1137/S1064827595289108.

[73] P. Virtanen, R. Gommers, T. E. Oliphant, M. Haberland, T. Reddy, D. Cournapeau, E. Burovski, P. Peterson, W. Weckesser, J. Bright, S. J. van der Walt, M. Brett, J. Wilson, K. J. Millman, N. Mayorov, A. R. J. Nelson, E. Jones, R. Kern, E. Larson, C. J. Carey, l. Polat, Y. Feng, E. W. Moore, J. VanderPlas, D. Laxalde, J. Perktold, R. Cimrman, I. Henriksen, E. A. Quintero, C. R. Harris, A. M. Archibald, A. H. Ribeiro, F. Pedregosa, P. van Mulbregt, A. Vijaykumar, A. P. Bardelli, A. Rothberg, A. Hilboll, A. Kloeckner, A. Scopatz, A. Lee, A. Rokem, C. N. Woods, C. Fulton, C. Masson, C. Häggström, C. Fitzgerald, D. A. Nicholson, D. R. Hagen, D. V. Pasechnik, E. Olivetti, E. Martin, E. Wieser, F. Silva, F. Lenders, F. Wilhelm, G. Young, G. A. Price, G.-L. Ingold, G. E. Allen, G. R. Lee, H. Audren, I. Probst, J. P. Dietrich, J. Silterra, J. T. Webber, J. Slavič, J. Nothman, J. Buchner, J. Kulick, J. L. Schönberger, J. V. de Miranda Cardoso, J. Reimer, J. Harrington, J. L. C. Rodríguez, J. Nunez-Iglesias, J. Kuczynski, K. Tritz, M. Thoma, M. Newville, M. Kümmerer, M. Bolingbroke, M. Tartre, M. Pak, N. J. Smith, N. Nowaczyk, N. Shebanov, O. Pavlyk, P. A. Brodtkorb, P. Lee, R. T. McGibbon, R. Feldbauer, S. Lewis, S. Tygier, S. Sievert, S. Vigna, S. Peterson, S. More, T. Pudlik, T. Oshima, T. J. Pingel, T. P. Robitaille, T. Spura, T. R. Jones, T. Cera, T. Leslie, T. Zito, T. Krauss, U. Upadhyay, Y. O. Halchenko, Y. Vázquez-Baeza, and S. . Contributors, Scipy 1.0: fundamental algorithms for scientific computing in python, Nature Methods **17**, 261 (2020).

[74] R. Erban, J. Chapman, and P. Maini, A practical guide to stochastic simulations of reaction-diffusion processes (2007).

[75] A. Goldbeter, Oscillatory enzyme reactions and Michaelis–Menten kinetics, FEBS Letters **587**, 2778 (2013), a century of Michaelis-Menten kinetics.

[76] H. Shankaran and H. S. Wiley, Oscillatory dynamics of the extracellular signal-regulated kinase pathway, Current Opinion in Genetics & Development **20**, 650 (2010), genetics of system biology.

[77] P. Kraikivski, Glycolytic oscillations, in *Case Studies in Systems Biology* (Springer International Publishing, Cham, 2021) Chap. Glycolytic Oscillations, pp. 59–68.

[78] M. S. Alnæs, J. Blechta, J. Hake, A. Johansson, B. Kehlet, A. Logg, C. Richardson, J. Ring, M. E. Rognes, and G. N. Wells, The FEniCS Project Version 1.5, Archive of Numerical Software **3**, 9 (2015).

[79] https://github.com/ruizbaier/closestMolecule.

[80] A. Ern and J.-L. Guermond, *Theory and Practice of Finite Elements* (Applied Mathematical Sciences, 159. Springer-Verlag, New York, 2004).

[81] V. Ervin, Approximation of axisymmetric Darcy flow using mixed finite element methods, SIAM Journal on Numerical Analysis **51**, 1421 (2013).

[82] G. Baird, R. Bürger, P. E. Méndez, and R. Ruiz-Baier, Second-order schemes for axisymmetric Navier–Stokes–Brinkman and transport equations modelling water filters, Numerische Mathematik **147**, 431 (2021).

[83] M. Neilan and A. Zytoon, Low-order Raviart–Thomas approximations of axisymmetric Darcy flow, Journal of Mathematical Analysis and Applications **473**, 905 (2019).

[84] C. Bernardi, M. Dauge, Y. Maday, and M. Azaıez, Spectral methods for axisymmetric domains, series in applied mathematics 3, Gauthier–Villars & North-Holland, Elsevier, Paris (1999).

[85] E. Burman and A. Ern, Continuous interior penalty *hp*-finite element methods for advection and advection-diffusion equations, Mathematics of Computation **76**, 1119 (2007).

[86] P. B. Bochev, M. D. Gunzburger, and J. N. Shadid, Stability of the SUPG finite element method for transient advection–

diffusion problems, Computer Methods in Applied Mechanics and Engineering **193**, 2301 (2004).

[87] E. Burman and C. He, Primal dual mixed finite element methods for indefinite advection-diffusion equations, SIAM Journal on Numerical Analysis **57**, 2785 (2019).